195

Evaluation of forecast error covariance matrix

F. Rabier and A.P. McNally

Research Department

September 1993

1. INTRODUCTION

Statistical analysis schemes combine observations with a background consisting of a short-range forecast, taking into account their respective error statistics. The background error statistics are absolutely crucial to determine the intensity and the spread of the increments brought by the observations. The forecast error for any meteorological field ψ can be noted $\psi_b - \psi_t$, where ψ_b and ψ_t are vectors representing respectively the background field and the true state. This paper re-addresses the problem of specifying forecast error characteristics.

Two basic quantities describing the statistics of $\psi_b - \psi_t$ are the mean vector and the covariance matrix: $E = \overline{\psi_b - \psi_t}$, $V = \overline{(\psi_b - \psi_t)(\psi_b - \psi_t)^T}$. The mean E is generally taken as 0, and the covariance matrix V is split between variances, horizontal and vertical correlations. Moreover, for the horizontal correlations, one makes the assumption of homogeneity and isotropy. The useful information then reduces to a single function of distance $f(r)$.

The current statistics used in OI are based on observational studies (*Hollingsworth and Lönnberg*, 1986; *Lönnberg and Hollingsworth*, 1986, hereafter denoted HL86 and LH86; *Lönnberg*, 1988) in which statistics are accumulated over the Northern American radiosonde network. The horizontal auto-correlation function is fitted by a series of Bessel functions: $f(r) = \sum_{n=0}^{N} \phi_n^2 J_o (k_n \frac{r}{d})$. The horizontal extent of the USA is 3000 to 4000 km and so this method gives information for equivalent spherical total wave number greater than **9** to **12**. It does not give useful information in the range [0,10]. This is not critical in OI because it uses data over a limited area at a time, but in 3DVAR, information about this large-scale component of the background error correlation had to be provided. Philippe Courtier proposed a parametric formulation for the auto-correlation wind spectrum (Memo R43.12/PC/CE/245, 9 October 1992) and Bill Heckley showed how untuned parameters could lead to spurious large-scale increments (Memo R43.12/WH/293/DA). Attempts are made to improve the specification of large-scale forecast error correlations.

The same statistics from HL86 and LH86 were used to derive vertical correlation functions for the OI. However, recent studies from 1D-VAR suggest the specification of these functions determines the success or otherwise of attempts to assimilate satellite radiance data. This will also be important in 3D-VAR, and so vertical correlations are also investigated.
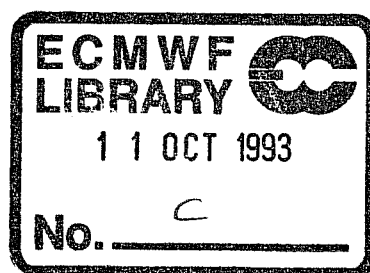
2. LARGE-SCALE COMPONENT OF THE BACKGROUND ERROR CORRELATION ESTIMATED FROM SATELLITE DATA

2.1 The method

To determine objectively the large-scale contribution of background error correlation using observed increments, global data coverage is needed. Satellite data are the most appropriate data source to be used for this purpose. The radiance measured in a particular satellite channel is effectively a weighted average of the temperature profile T(z)

$$R = \int_z B(T(z)) \frac{d\tau(z)}{dz} dz$$

Thus calculating radiances from the model and comparing to measured values allows an "observation" of model error in this vertically averaged space. Fig 1 shows the extent of this vertical averaging process for the TOVS channels used in this study, the results of which are presented in section 2.2. Departure fields in brightness temperature from PRESAT output files are used. A departure field is written as $\psi_b - \psi_o$, where ψ_b is the background field and ψ_o the observation. In the following, we will denote $\overline{X}$ and σ_X the empirical mean and standard deviation of a field X. The basic assumption is that, once the departure has

been properly normalized: $(\psi_b - \psi_o)' = \dfrac{\psi_b - \psi_o - \overline{(\psi_b - \psi_o)}}{\sigma_{\psi_b - \psi_o}}$, its spatial correlations reflect the spatial

correlation of the forecast error $(\psi_b - \psi_t)'$ (actually, it represents the forecast error correlation multiplied by a constant, where the constant measures the ratio of background error to total error (background and observation)). This should be true, at least in the large scale, where observation error correlations between the radiances themselves may be ignored. Clear data from NOAA11 and NOAA12 over both land and sea are used. These data are bias-corrected using an air -mass dependent procedure to remove the bias between model and observation (*Eyre, 1992*). This should further remove any chance of radiance correlations contaminating the results (remark: the bias correction is applied separately for each satellite).

Statistics are computed for two different periods (October 1992 and February 1989). Separate departure fields for 0,6,12,18 UTC are interpolated using a three pass Cressman analysis to produce global fields on a grid of 160 latitudes and 320 longitudes (radii of 5,3 and 1 grid points around each observation are used in the analysis, but the result is not sensitive to this choice for large scale features). The empirical mean $\overline{\psi_b - \psi_o}$ and standard deviation $\sigma\psi_b - \psi_o$ are computed at each grid-point for each of the four 6-hour slots of the 44 (October 92) and 48 (February 89) departure fields which could be successfully analyzed (i.e. had good data coverage). The departure fields are then normalized by removing the mean and dividing by the standard-deviation.
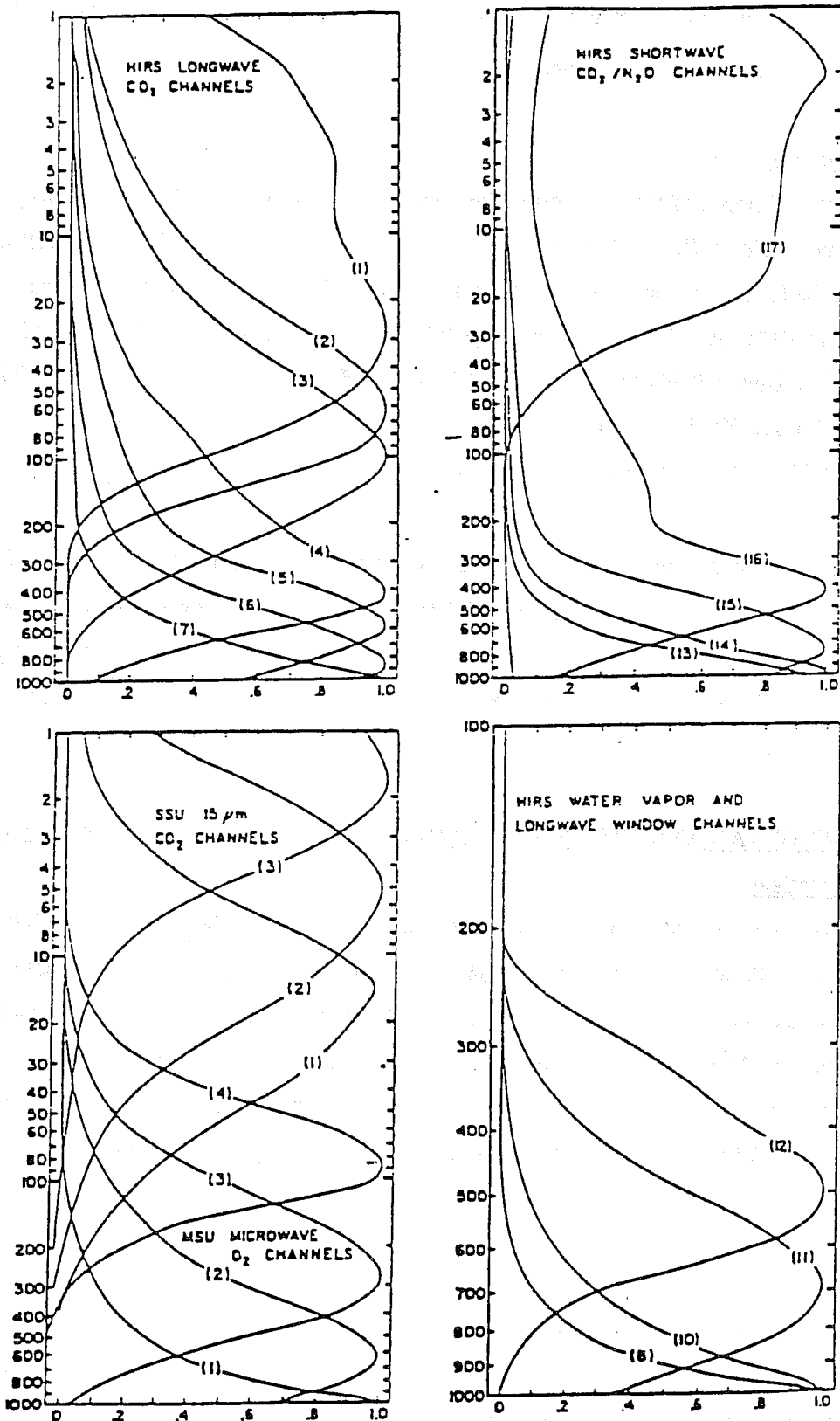
Fig 1   TOVS weighting functions.

For each realisation i, the normalized departure field $(Di(\lambda,\mu))\lambda,\mu$ is then transformed in spectral space $(Di(n,m))_{n,m}$. The computation of the correlation spectra and their relationship to spectra with respect to Bessel functions are described in the appendix.

2.2 The results

Results in terms of slopes of the auto-correlation function agree to within 10% for the two periods, except for those derived using MSU 4 which gives the noisiest results. Results for February 1989 were generally smoother, as the limb correction was applied to the satellite data for this data set whereas it was not done for the October 1992 data. Results for February 1989 and for 6 channels are presented. Fig 2.a shows the spectrum derived from MSU4 (peaking at 70-100 hPa), 2.b HIRS4 (peaking at 400 hPa), 2.c MSU2 (peaking at 600-700 hPa), 2.d HIRS15 (peaking at 700-800 hPa), 2.e HIRS13 (peaking at the ground) and 2.f for HIRS 11 (humidity channel peaking at 700 hPa).

The corresponding large-scale slopes (n – 2 to 10, typically) are 0 for MSU4, 0.4 for HIRS4, 0.5 for MSU2, 0.5 for HIRS15, 0.6 for HIRS13, and 0.6 for HIRS11. The stratospheric channel MSU4 exhibits a rather flat spectrum at large-scale (in fact, the spectrum is hardly regular enough to give a significant slope different from 0). In the tropospheric channels, slopes increase from 0.4 in the upper troposphere to 0.6 in the lower troposphere.

3. HORIZONTAL AND VERTICAL CORRELATIONS DERIVED FROM NMC'S METHOD

3.1 The method

The basic strategy of the NMC method is to accumulate statistics of the differences between forecasts at different ranges valid at the same time (*Parrish and Derber*, 1992). The assumption behind the method is that the differences between these forecasts represent forecast error. For this study the method is applied to comparisons of 24 and 48 hour forecast fields valid at 12 UTC on the same day. This choice is somewhat arbitrary, but using the 24 hour forecast as a validation avoids any problems associated with spin-up. It also allows differences to be examined over 24 hours, a period not too long in order for the error not to be significantly different from a 6 hour forecast error, and not too short that the forecasts are too similar because of the lack of update by data.

The truncation selected for the computations was T106 L31 and operational forecasts were compared for December 1992. As a first step, the covariance computation was performed directly in spectral space. The mean error field is a full spectral field (locally varying mean) which is removed from each departure field. However, for the necessary division by the standard-deviations to go to correlation matrices, the variances were globally averaged at each level. This is of course a slight approximation, but is believed to be sufficient.
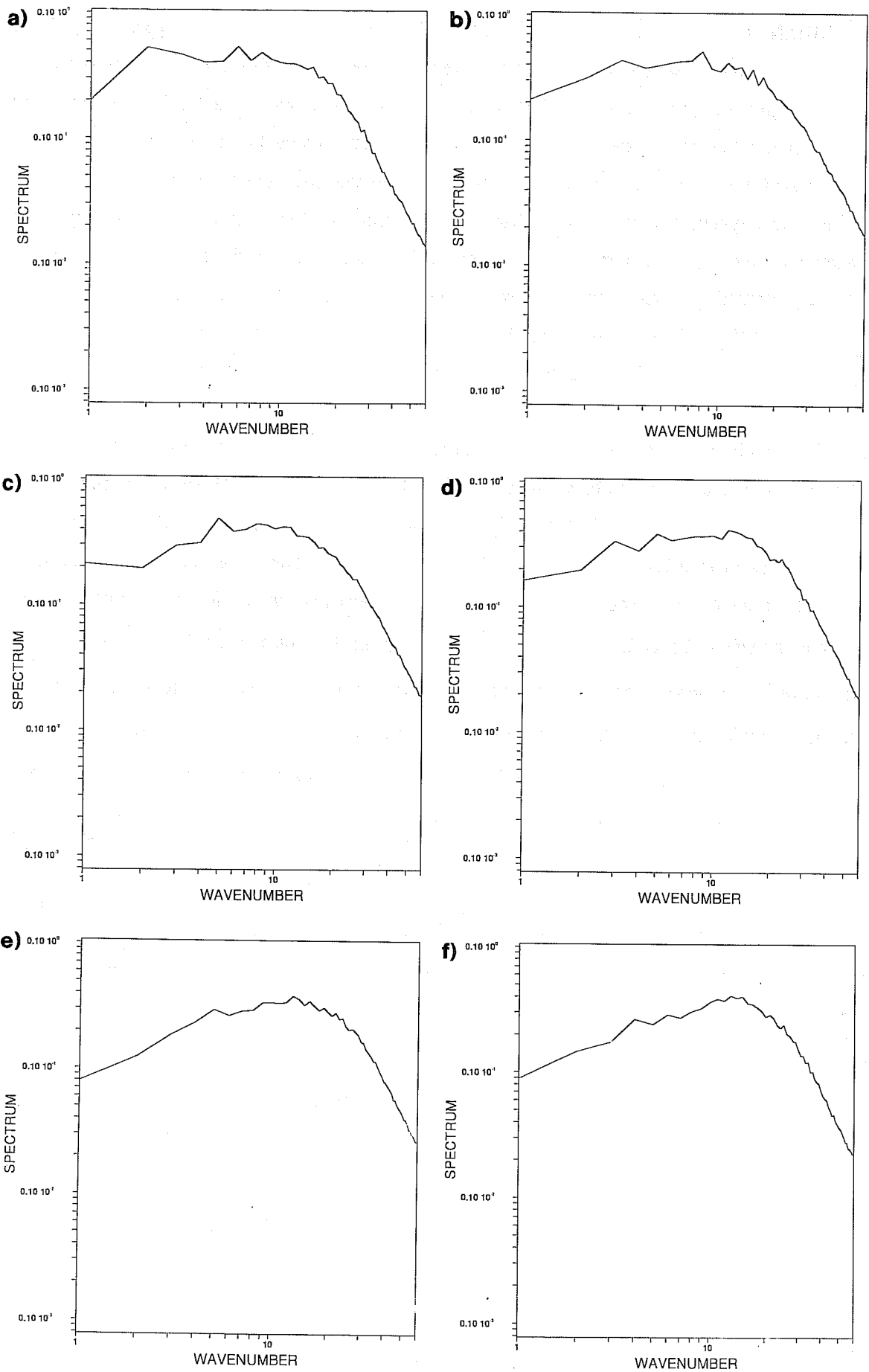
Fig 2   Autocorrelation spectra of first-guess minus observations for channels (a) MSU4, (b) HIRS4, (c) MSU2, (d) HIRS15, (e) HIRS13 and (f) HIRS11.

3.2   The horizontal correlations

Horizontal covariances were examined for each vertical level. Fig 3 shows the variance spectra for wind (3.a) and temperature (3.b) at levels 1 (dotted line), 18 (dashed line) and 31 (solid line). It can be seen from the slopes that in the small-scales much more energy is present in model error close to the ground than high in the stratosphere. In the large scales the differences between the slopes are more subtle. However, for the temperature spectra one can notice a slightly steeper slope for lower levels, which is in agreement with the results obtained from the radiances in section 2. In figures 4 and 5, the autocorrelation spectra for all levels are presented in terms of wind and temperature respectively, for levels 1 to 10 (Fig 4.a and Fig 5.a), levels 11 to 20 (Fig 4.b and 5.b), levers 21-30 (Fig 4.c and 5.c). The top levels show more dispersion, particularly in the small-scale (where there is less energy at the very top of the model).

Most of the variation of the shape of the spectrum and then of the length-scale is concentrated in the stratosphere as previous studies have already shown (HL86 and LH86). Three representative levels have been chosen: levels 6 (around 100 hPa), 16 (around 400 hPa) and 26 (around 850 hPa). Autocorrelation spectra are presented in Fig 6, where level 6 is represented by a dotted line, level 16 by a dashed line and level 26 by a solid line. The spectra at these levels were reproduced for the departures between an initialized analysis and a 24 hour forecast (figure 7). For each of these spectra, we computed n_{max} which is the wavenumber where the spectrum reaches its maximum, the length-scale in km, (defined as the component length-scale of HL86) and the slopes in the large-scale ($n = 2$ to 10), in the range ($n = 40$, $n = 70$), and in the range ($n = 70$, $n = 100$). Results are presented in the following table:

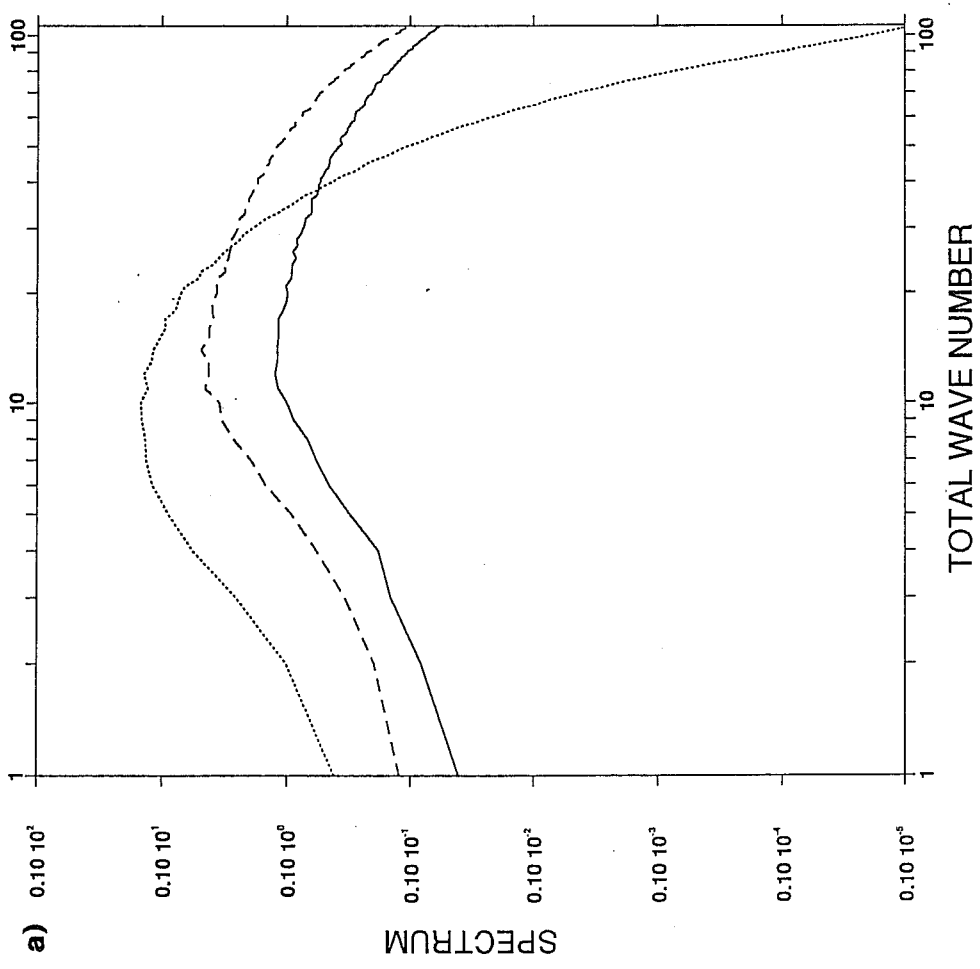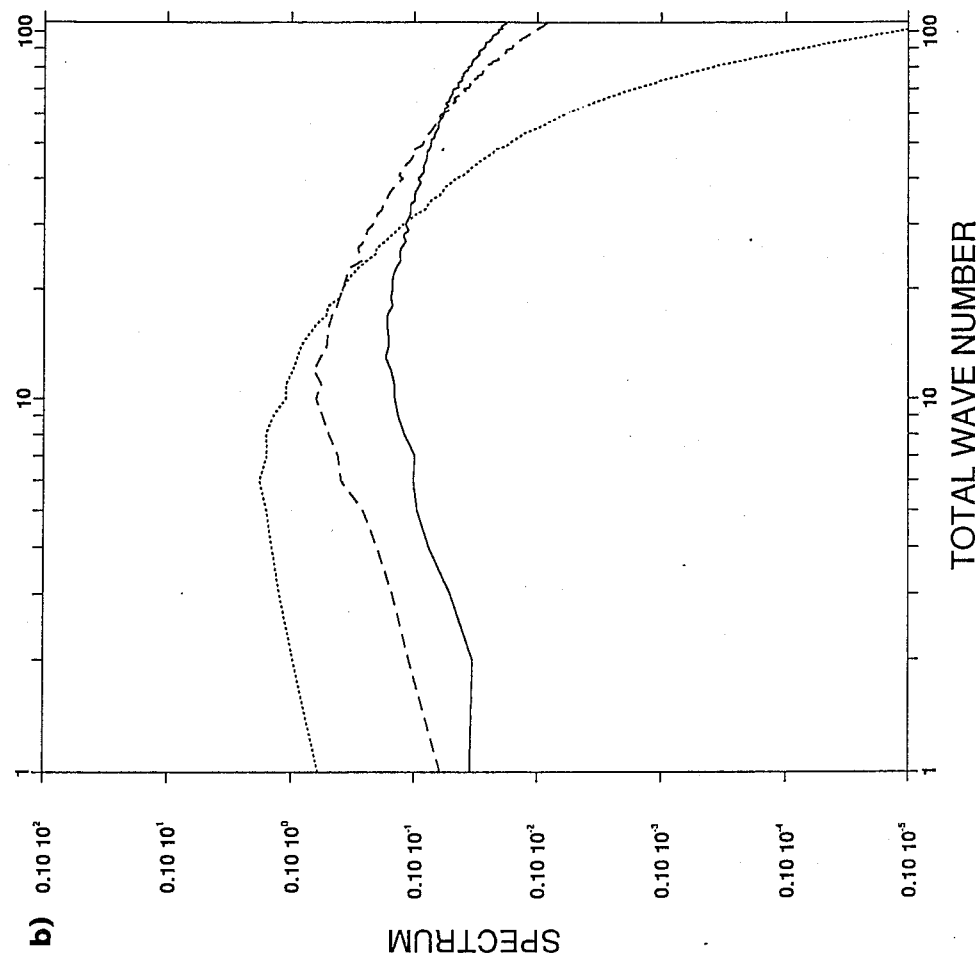|	max		Length-scale		Large-scale slope		Slope 40-70		Slope 70-100	
Level 6 (0-24) KE and T	10	8	288	292	0.91	0.35	-3.1	-2.3	-5.7	-4.9
Level 16 (0-24) KE and T	15	10	239	289	1.43	0.78	-2.4	-2.1	-3.4	-2.9
Level 26 (0-24) KE and T	16	12	241	262	1.37	0.85	-2.5	-1.7	-2.8	-2.5
Level 6 (24-48) KE and T	9	10	299	299	1.38	0.64	-2.9	-2.6	-6.0	-5.2
Level 16 (24-48) KE and T	14	10	238	275	2.24	0.91	-2.2	-2.1	-3.9	-3.6
Level 26 (24-48) KE and T	12	10	232	236	1.80	0.94	-2.0	-1.9	-3.3	-3.1

Fig 3   Variance spectra for differences between 24hr and 48hr forecasts at model levels 1 (dotted line), 18 (dashed line) and 31 (solid line), for (a) wind and (b) temperature.
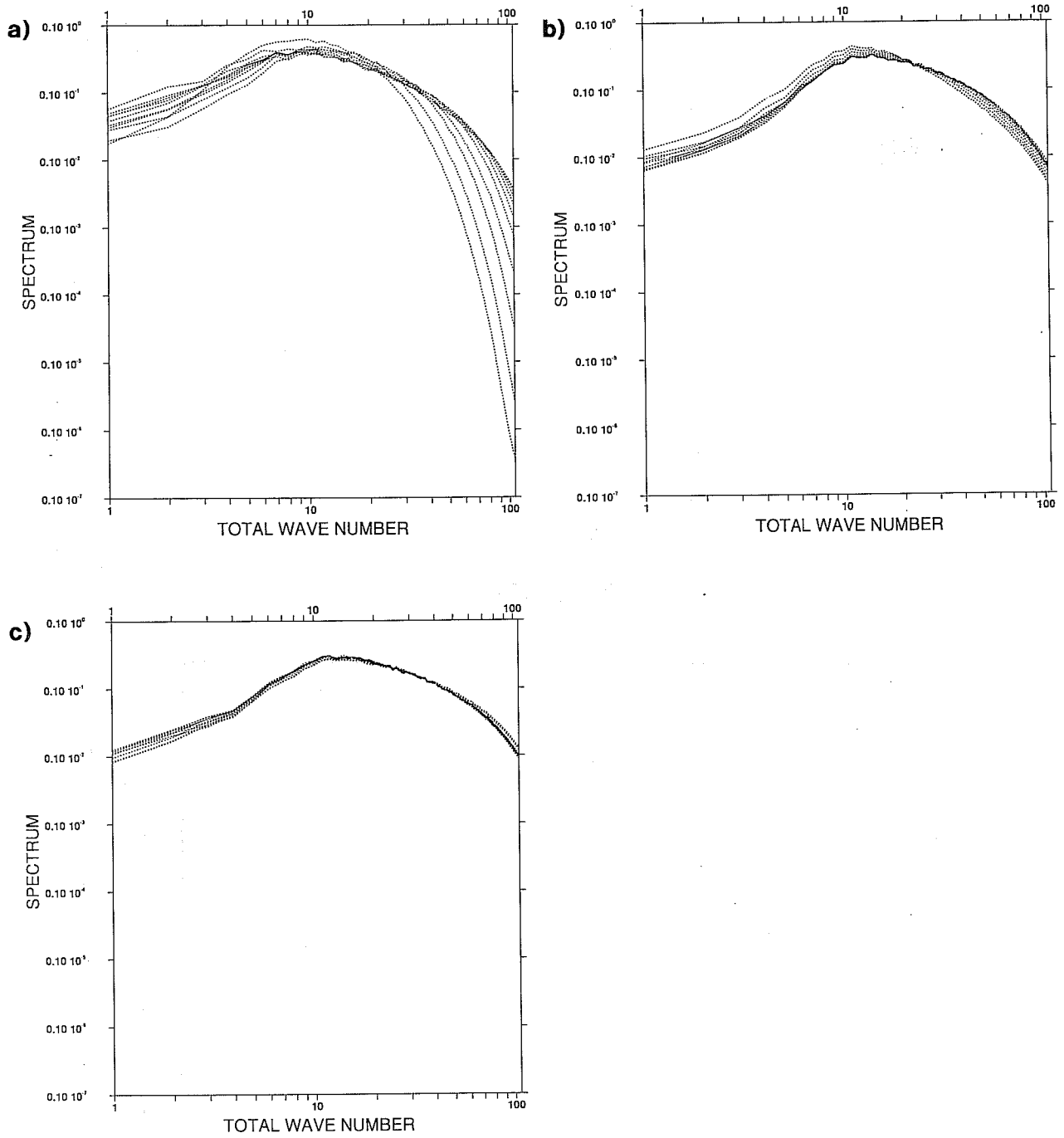
a)

b)

c)

Fig 4   Autocorrelation spectra for wind differences between 24hr and 48hr forecasts, for model levels
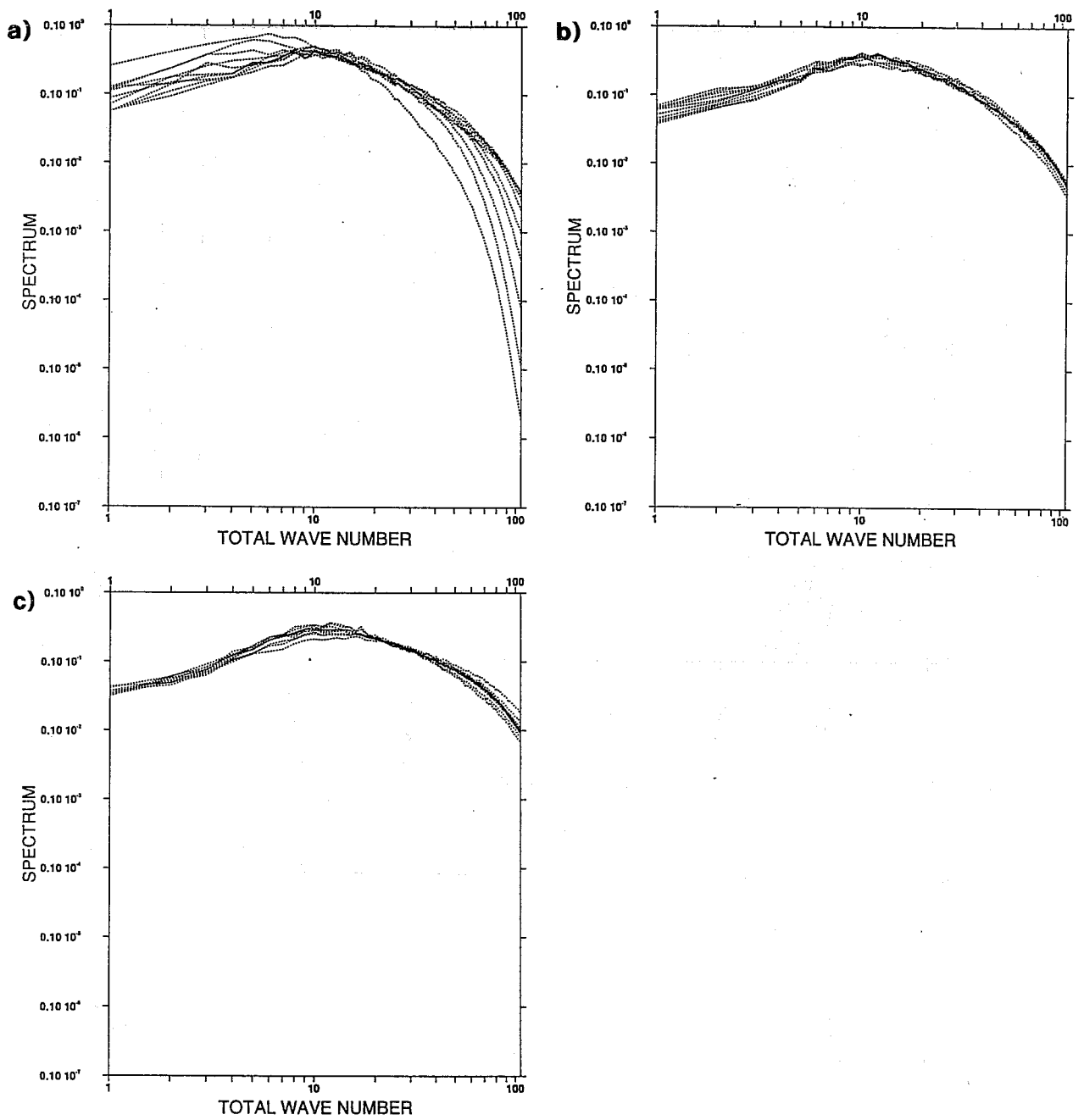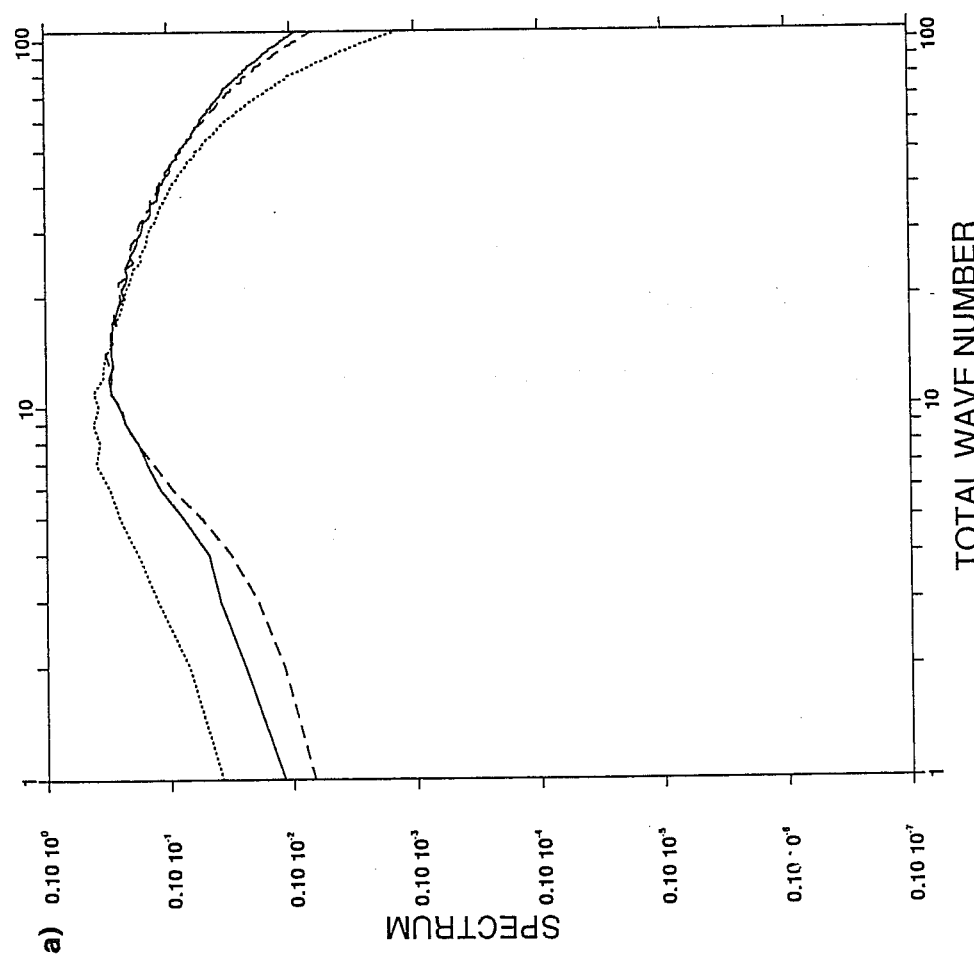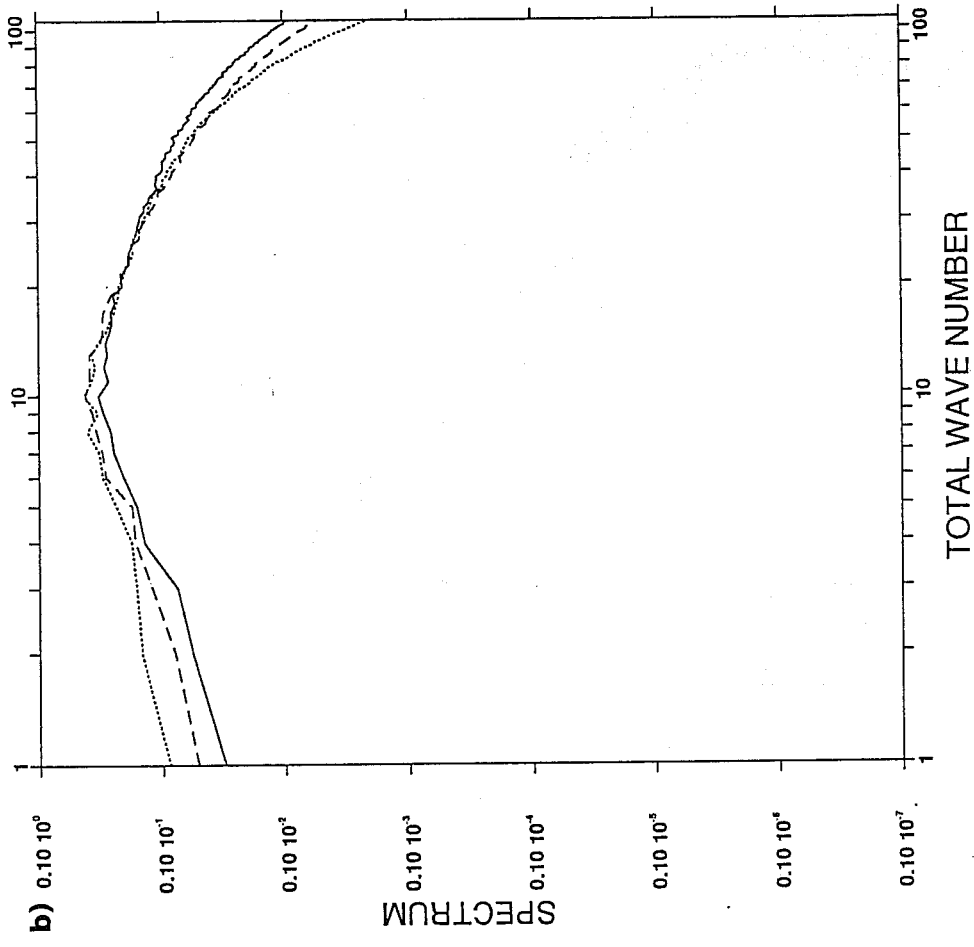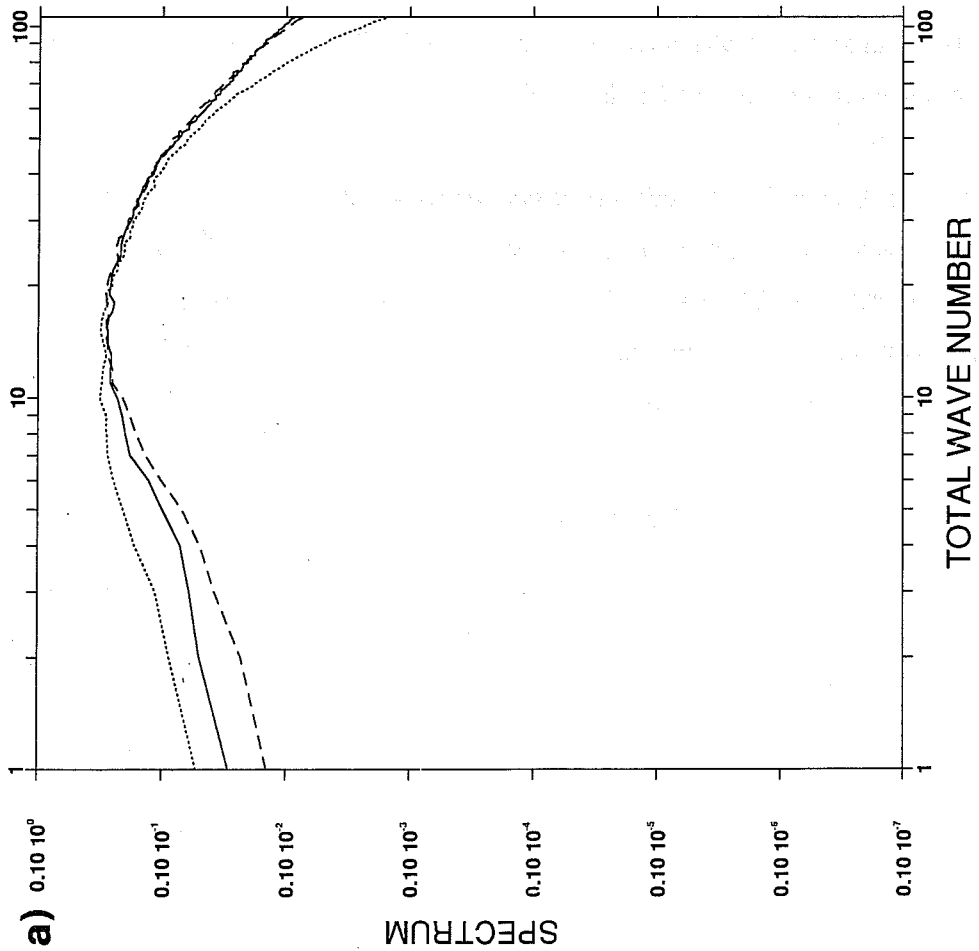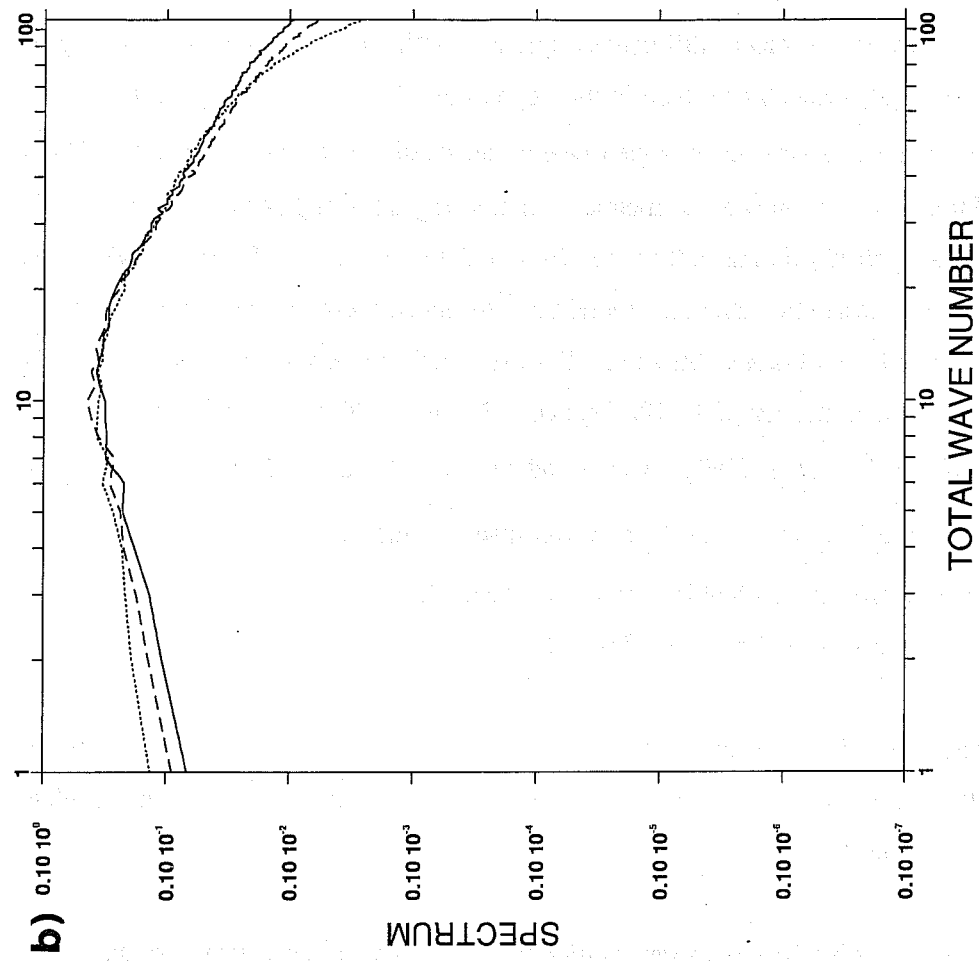(a) 1 to 10, (b) 11 to 20 and (c) 21 to 30.

Fig 5   Autocorrelation spectra for temperature between 24hr and 48hr forecasts, for model levels
(a) 1 to 10, (b) 11 to 20 and (c) 21 to 30.

Fig 6   Autocorrelation spectra for differences between 24hr and 48hr forecasts at model levels 6 (dotted line), 16 (dashed line) and 26 (solid line), for (a) wind and (b) temperature.

10

Fig 7   Autocorrelation spectra for differences between initialized analysis and 24hr forecast at model levels 6 (dotted line), 16 (dashed line) and 26 (solid line), for (a) wind and (b) temperature.

For both the 0-24 and 24-48 model differences, one can notice the predominance of large-scales in the stratosphere, with length-scales bigger than in the troposphere. A rather flat slope is seen in the very large scales (n - 2 to 10) and a very steep slope towards the small scales. For the slopes of the temperature spectra in the large scale one notices an increase when going from higher to lower levels. The slopes in the troposphere are typically around 0.8 for the 0-24 differences and 0.9 for the 24-48 differences. The results obtained from the satellite data are around 0.5. Although these results do not give exactly the same figure, they appear to be reasonably consistent. For the kinetic energy slope in the range 40-70 values are between -2 and -3 and in the range 70-100 between -3 and -6. These slopes agree well with the latest results of *Bartello and Mitchell* (1992) who found between -3 and -6 in terms of S_n spectrum which corresponds to -2 to -5 in terms of the P_n spectrum used in this study (see the appendix for definitions). The broader correlations at higher levels, which can be seen from the bigger length scales, are in agreement with previous observational results (HL86, Fig 13; LH86, Fig 6).

We have chosen to continue the study with the 24-48 differences. Although the results are not very different from the 0-24 differences, they are less likely to be contaminated with spin-up problems (it is what is currently used at NMC).

For the three representative levels chosen earlier (6,16 and 26), spectra were computed separately for vorticity and divergence. These spectra are shown in Fig 8 (a and b) and are quite different. The divergence errors are in smaller scales than the vorticity errors. The length-scale is 191 km as compared to 245 for the rotational part of the wind at level 16.

To check the degree of balance in the model errors derived with this method we also computed the 500 hPa variance spectra for wind and geopotential. These are presented in Fig 9 (a and b). The length-scales are respectively 239 and 493 km. The value of 493 km for the component length scale of the height auto-correlation agree well with what is currently used in OI (500 km in the latitude band 90N-30N) and correspond to what was initially chosen for 3DVAR.

The slopes for the wind and the geopotential spectra are respectively 1.9 and 0.9 for the range n - 2 to 10, -2.1 and -4.2 for the range n - 40 to 70, -3.8 and -5.2 for the range n - 70 to 100. The value of -4 for the geopotential in the range n - 40 to 70 is slightly steeper than what is actually used in OI (equivalent slope of -3, *Lönnberg*, 1988), but corresponds well to results in *Bartello and Mitchell* (1992). Furthermore, it is consistent with a geostrophic assumption, as there is a difference of -2 between the wind and the geopotential spectra slopes (see appendix for details).
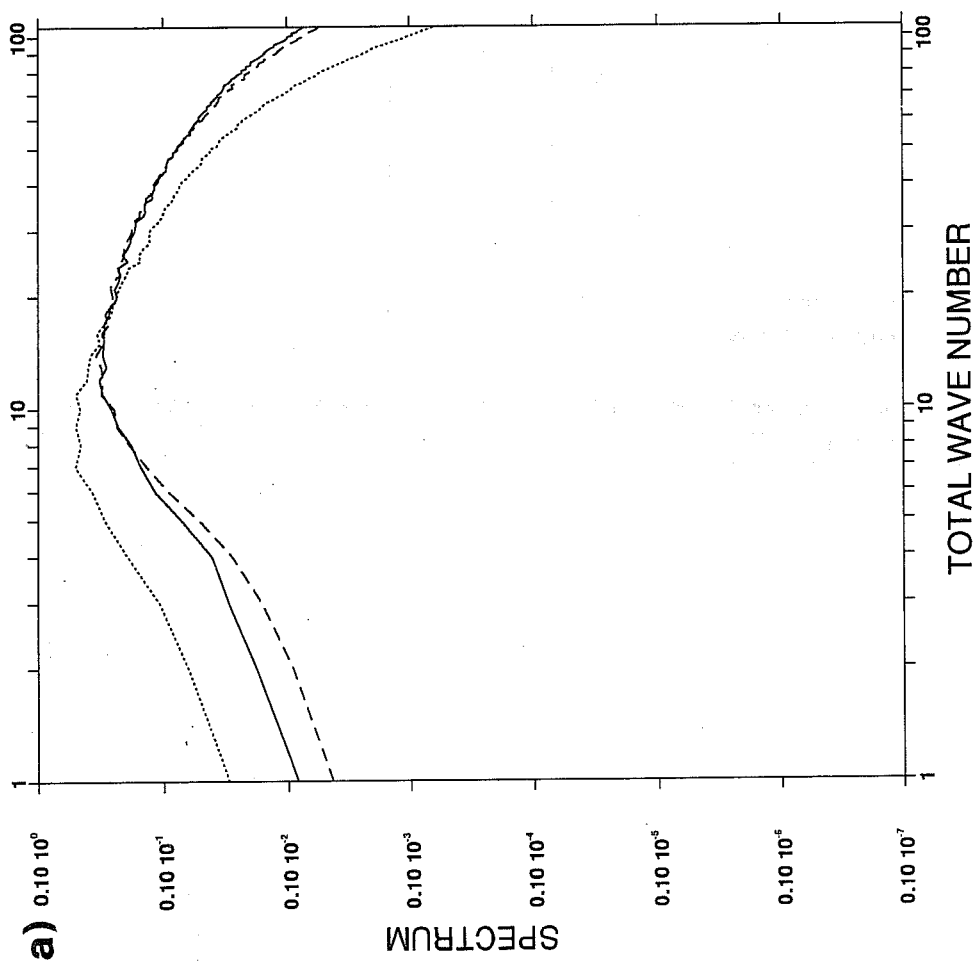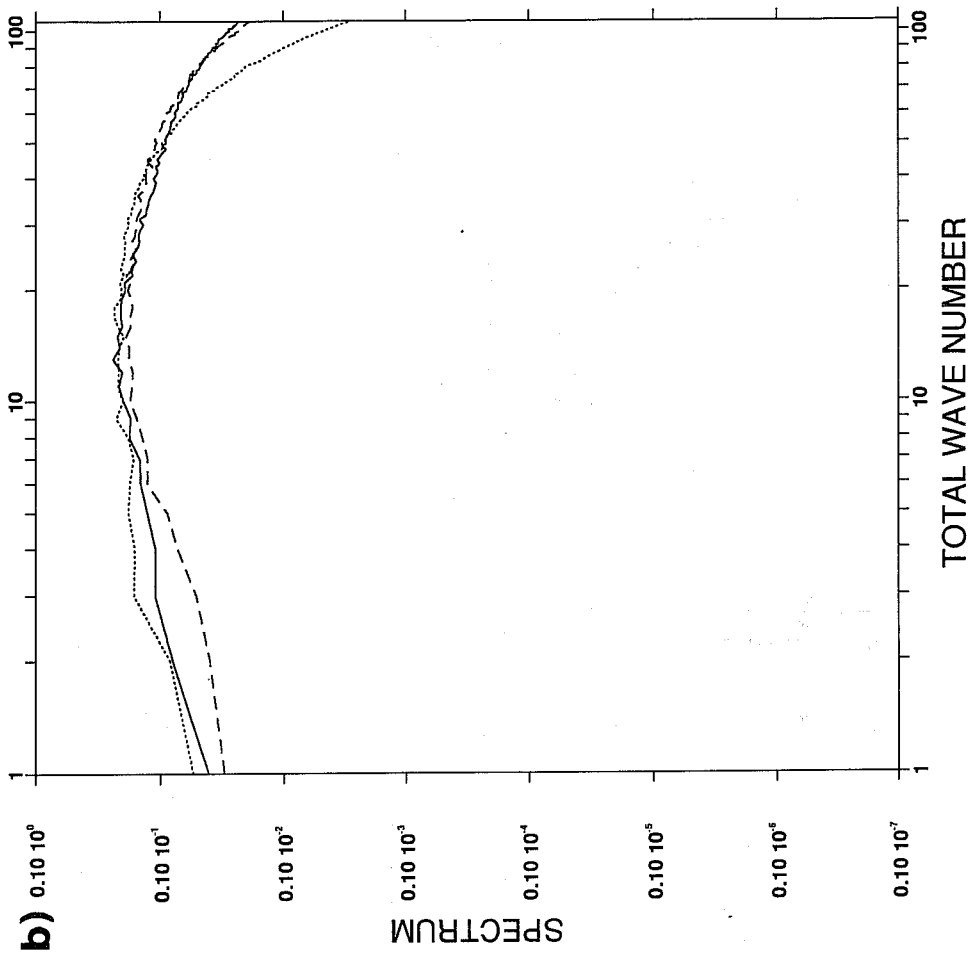
Fig 8 Autocorrelation spectra for differences between 24hr and 48hr forecasts at model levels 6 (dotted line), 16 (dashed line) and 26 (solid line), for (a) the rotational part of the wind and (b) the divergent part of the wind.
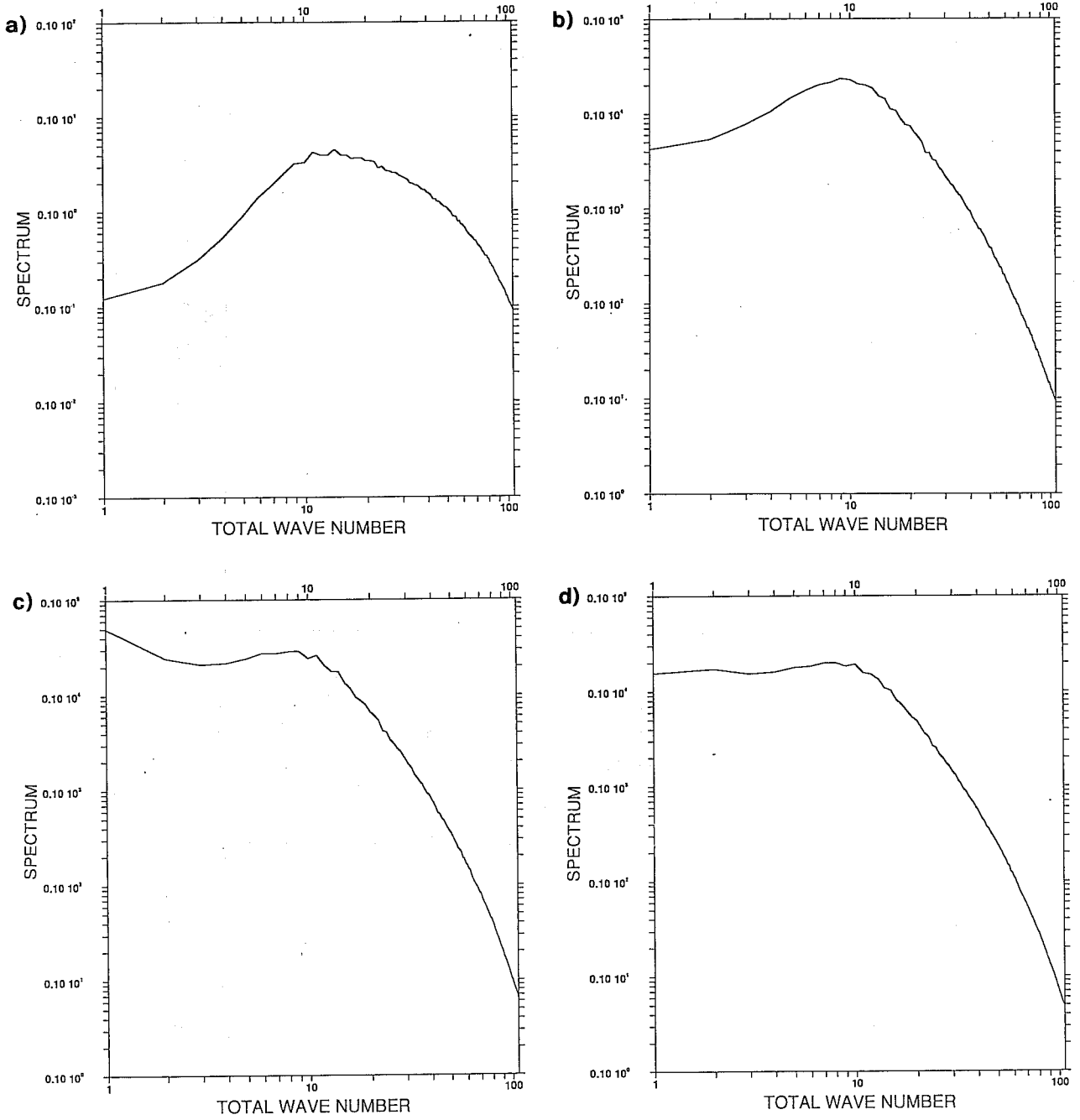
13

Fig 9   Variance spectra for differences between 24hr and 48hr forecasts for pressure level 500hPa, for
(a) wind, (b) geopotential, (c) geopotential computed from wind using geostrophic balance,
(d) geopotential computed from wind using linear balance.

This difference of -2 in the slopes does not apply exactly at smaller scales, or at all at large scales (1.8 and 0.9). Fig 9 (c and d) shows the geopotential variance spectra which would be obtained by applying both a geostrophic balance ($\phi = f\psi$) and a linear balance ($\Delta\phi = (\nabla . f)\nabla\psi$) to the wind spectra. All the geopotential spectra (i.e. observed, geostrophically balanced, linearly balanced) agree well in the range $n = 10$ to 100, but both balanced spectra disagree with the observed one in the range $n = 0$ to 10. Although the linearly balanced spectrum is in better agreement with the observed one than the simple geostrophically balanced spectrum, it is clear that we should apply a more elaborate relationship between balanced mass and wind increments at these large scales. On the whole, there is 10% less energy in the error variance for the balanced geopotential than for the observed one.

3.3   The vertical correlations

In the previous section, the spectra of the variances at each level i were given as

$$\sigma_i^2 = \sum_{n=0}^{N} \sum_{m=-n}^{n} \overline{\psi_n^m (Zi) \; \psi_n^m(Zi)^*}.$$

The covariance between levels Zi and Zj may be written

$$\text{Cov}(Zi, Zj) = \frac{1}{4\pi} \int_\lambda \int_\mu \overline{\psi(\lambda,\mu,Zi) \; \psi(\lambda,\mu,Zj)} d\lambda d\mu$$

$$\text{Cov}(Zi, Zj) = \sum_{n=0}^{N} \sum_{m=-n}^{n} \overline{\psi_n^m (Zi) \; \psi_n^m(Zj)^*}$$

and the corresponding correlations, dividing by globally averaged standard deviations are

$$C(Zi, Zj) = \frac{1}{\sigma_i \; \sigma_j} \text{Cov}(Zi, Zj).$$

The standard-deviations for height are compared with those from LH86 (column 1 below). The height statistics can be computed directly from pressure level geopotential fields (ϕ^2) (column 2) or can be deduced from the temperature statistics by the hydrostatic relationship, assuming no error in surface pressure (ψ_T^2) (column 3).

	$\sigma(\phi^2 obs)$	$\sigma(\phi^2)$	$\sigma(\phi_T^2)$
10 hPa	50 m	40 m	93 m
100 hPa	16 m	16 m	19 m
150 hPa	17 m	18 m	20 m
200 hPa	17 m	22 m	22 m
250 hPa	20 m	25 m	23 m
300 hPa	20 m	26 m	25 m
400 hPa	16 m	23 m	22 m
500 hPa	13 m	19 m	18 m
700 hPa	10 m	15 m	10 m
850 hPa	10 m	14 m	5 m
1000 hPa	10 m	16 m	1 m

(NB. the 10 hPa value for $\sigma(\phi^2 obs)$ is the one used in OI at mid-latitudes)

It can be seen that the computed values are slightly larger than those observed in HL86, but the three different sets of standard-deviations follow roughly the same vertical structure. A maximum at the top (10 hPa) is observed and a minimum at the lower levels. There is also a local maximum at 300 hPa and a local minimum at 100 hPa. Similarly, standard deviations for wind and temperature have been derived: they compare well with HL86/LH86.

Some discrepancies are visible between $\sigma(\phi^2)$ and $\sigma(\phi_T^2)$ at the top level and the two lower levels. These might be due to inaccuracies in the way we derive height statistics from temperature statistics, in particular, close to the ground where an error-free surface pressure is assumed. However, these differences in standard-deviation do not significantly affect the vertical correlations and it was decided to use the statistics derived from temperature as they are more continuous.

Fig 10 represents the vertical correlations for temperature (10.a), rotational part of the wind (10.b), divergent part of the wind (10.c) and geopotential (10.d).

The temperature results agree well with the vertical correlations derived from background-radiosonde statistics shown in Fig 11.a (previously used in 1D-VAR, see *McNally*, 1993) and with those from HL86 (derived from thicknesses) reproduced for convenience in Fig 11.b.
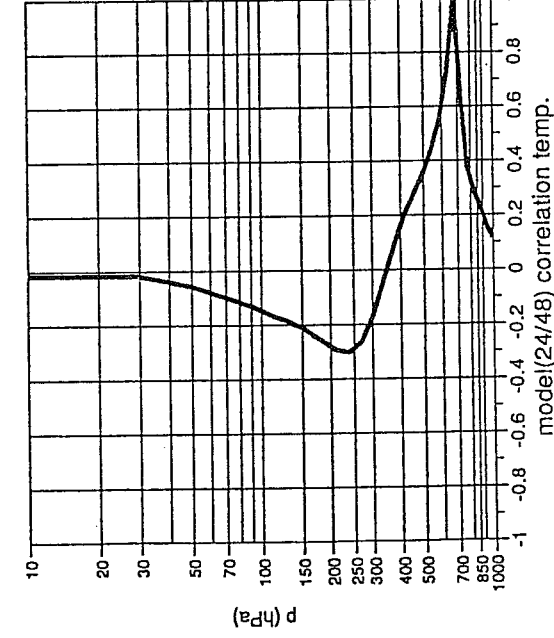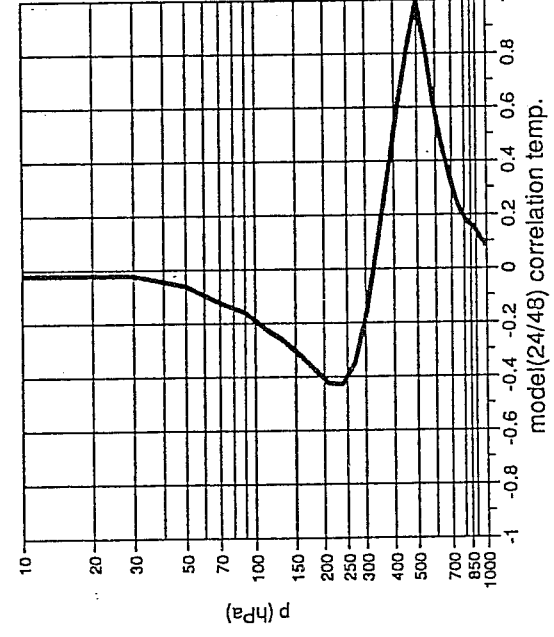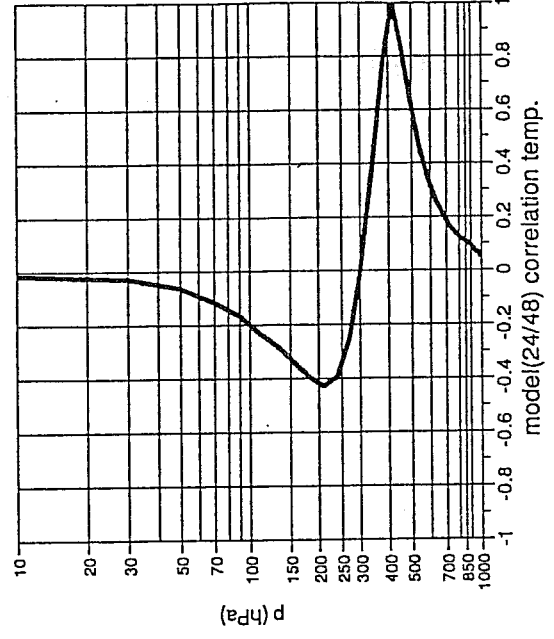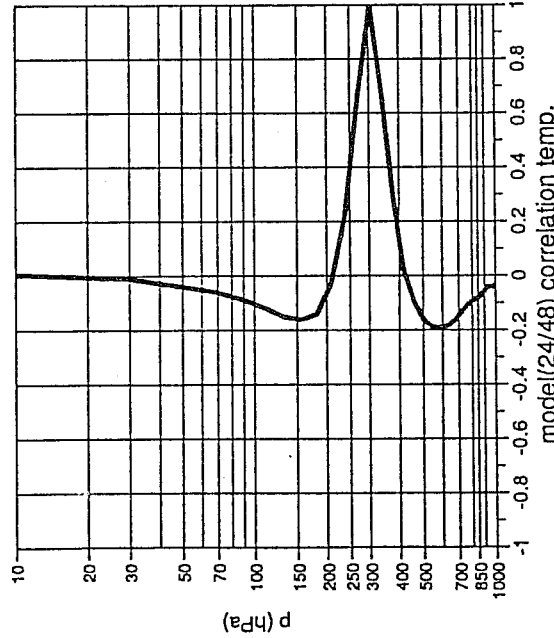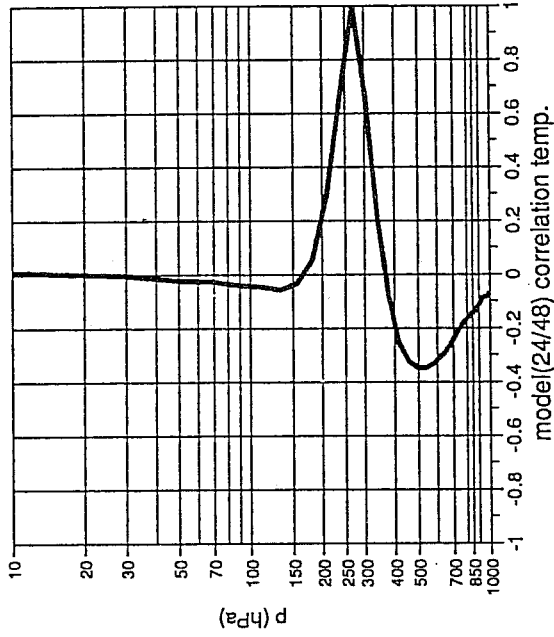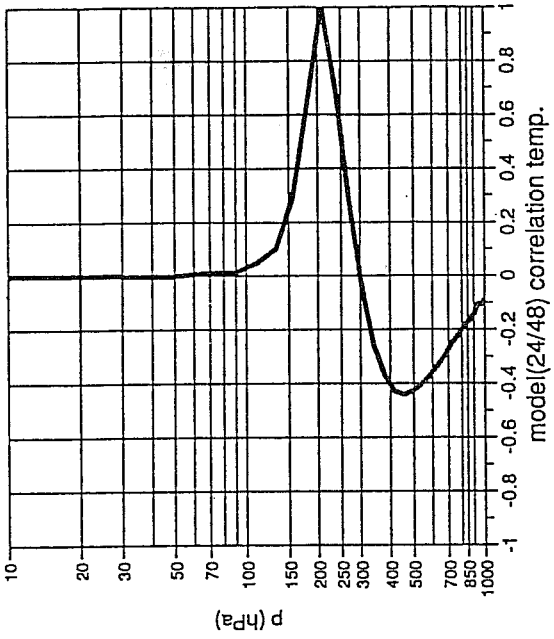
Fig 10(a) Vertical correlations for differences between 24hr and 48hr forecasts for different levels, for temperature.

17
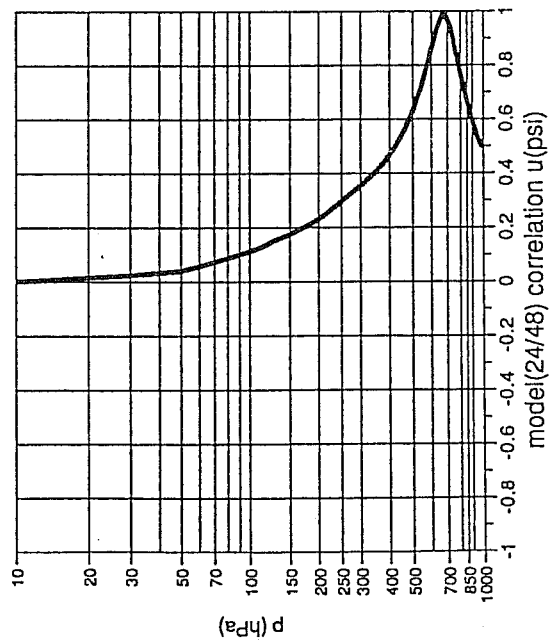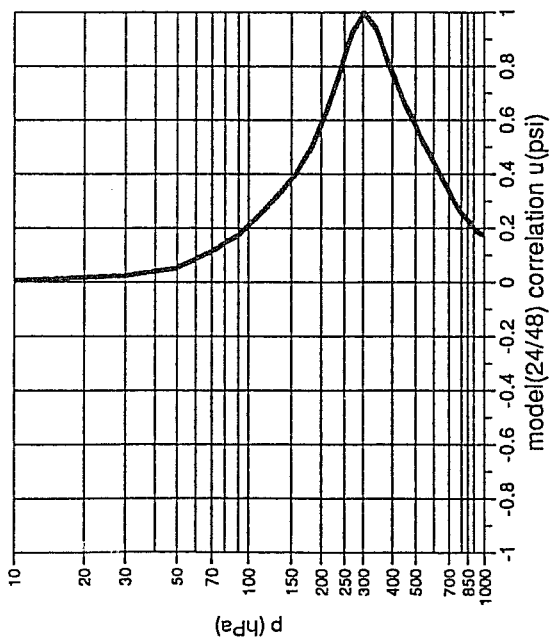
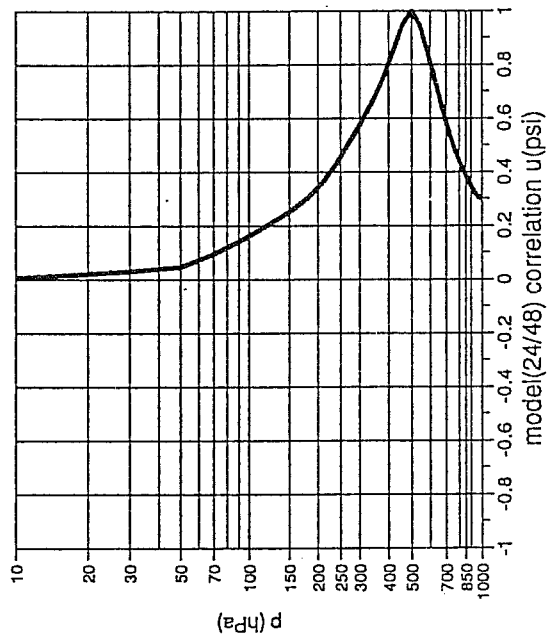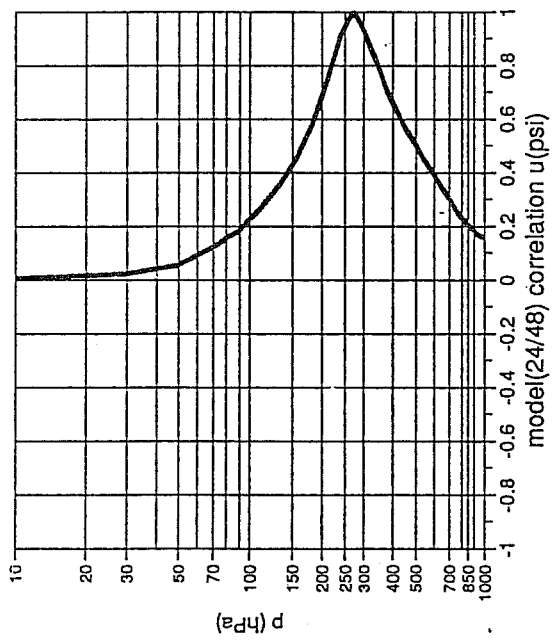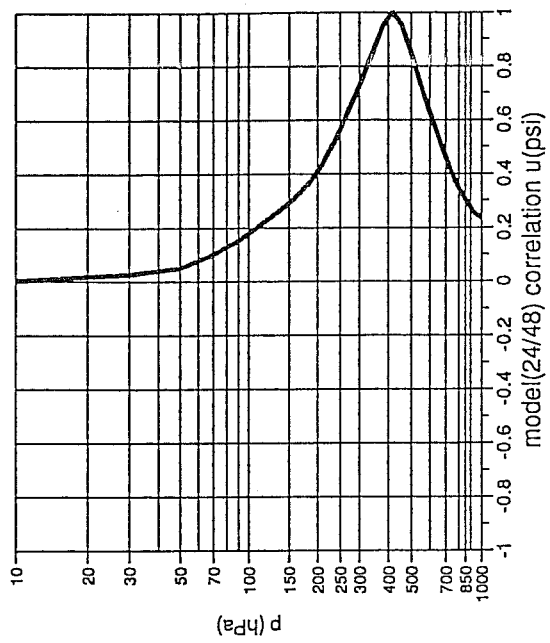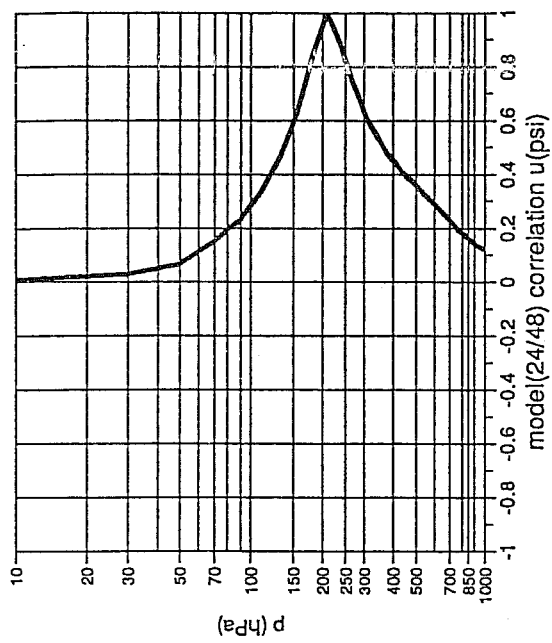Fig 10(b) Vertical correlations for differences between 24hr and 48hr forecasts for different levels, for rotational part of the wind.
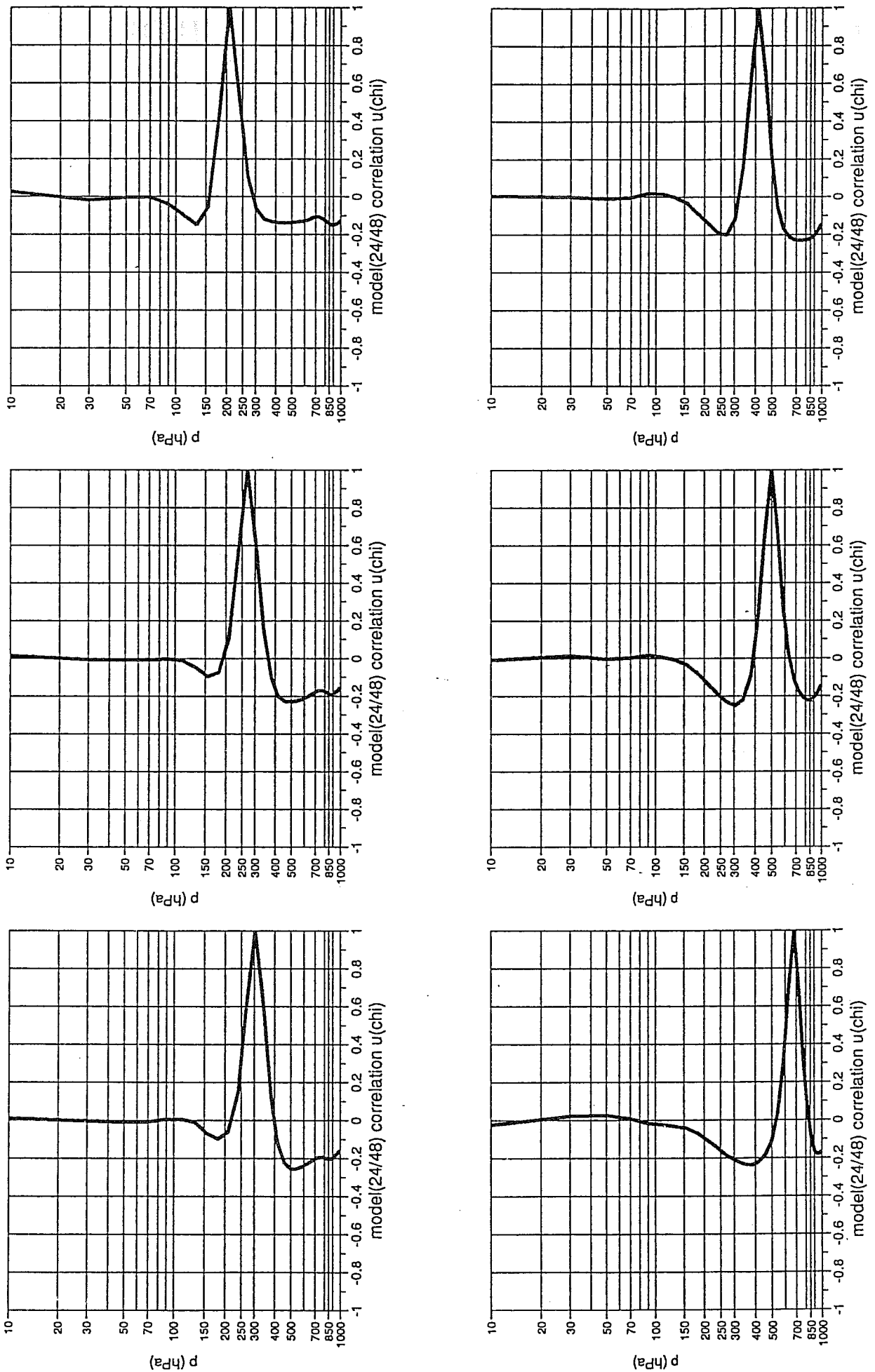
18

Fig 10(c) Vertical correlations for differences between 24hr and 48hr forecasts for different levels, for divergent part of the wind.
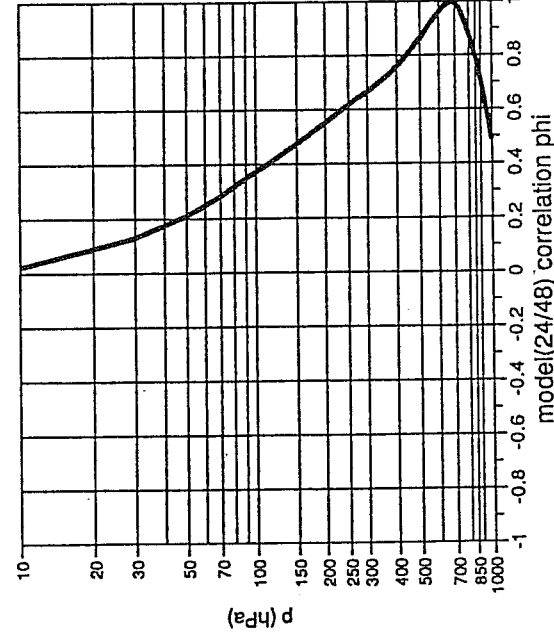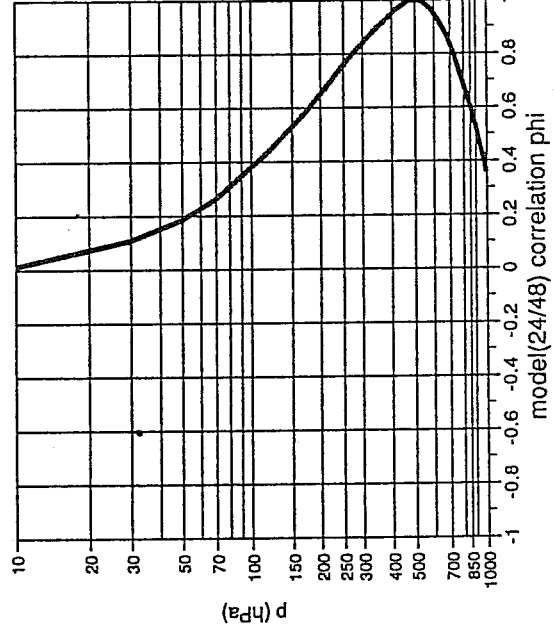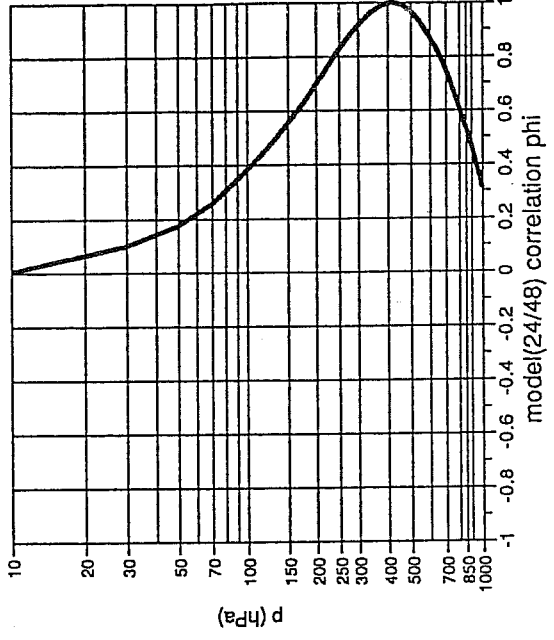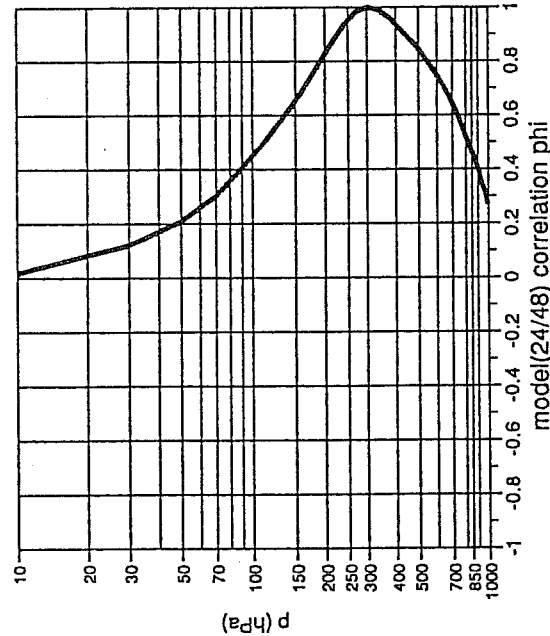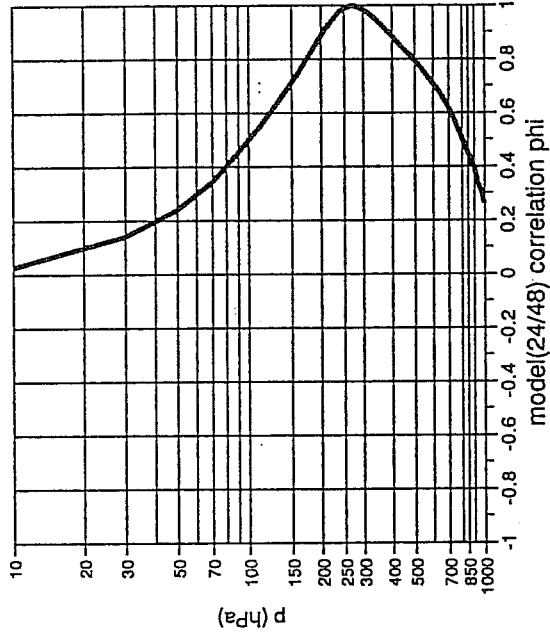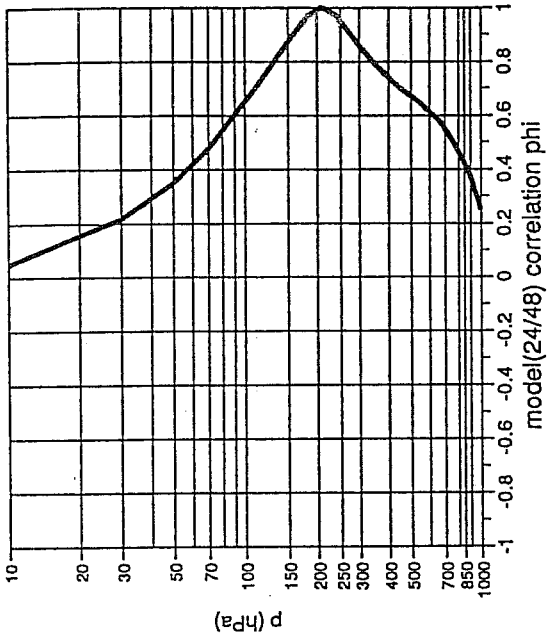
19

Fig 10 (d) Vertical correlations for differences between 24hr and 48hr forecasts for different levels, for geopotential.

20

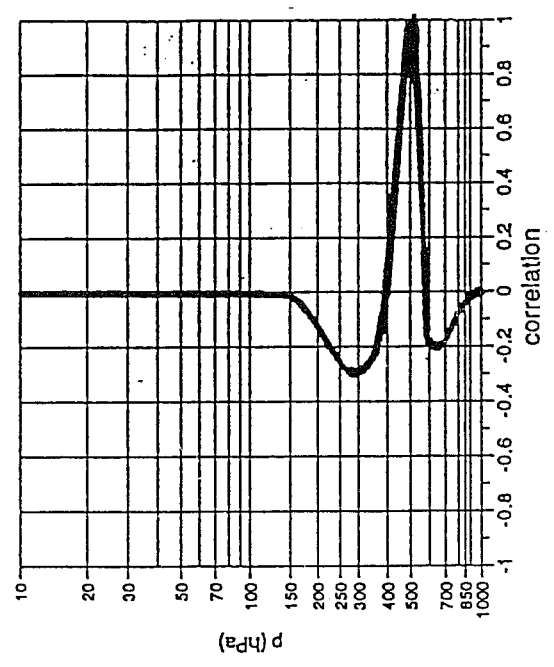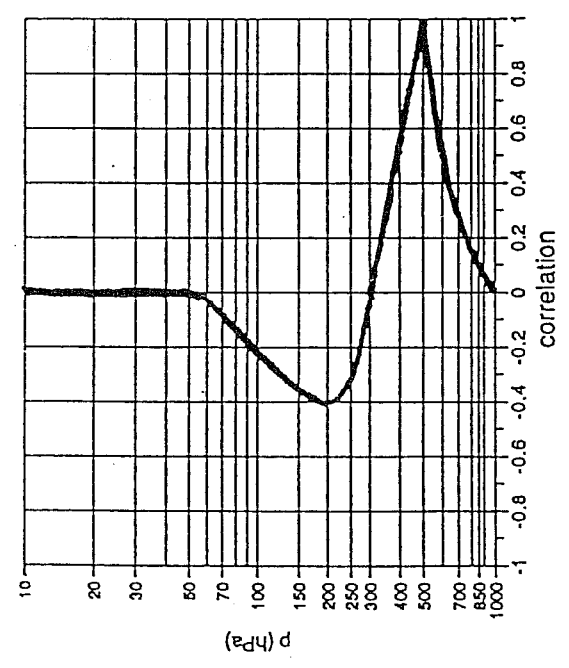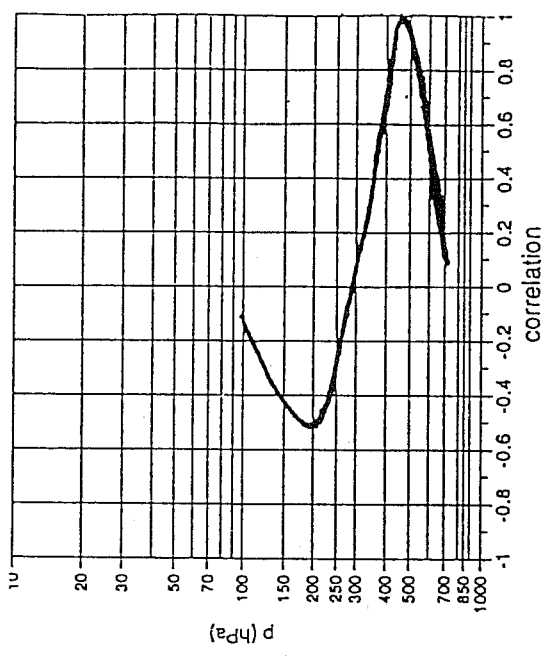Fig 11 Vertical correlations for temperature errors for level 500 hPa, (a) as previously used in 1D-VAR, (b) as computed from thicknesses departures in LH86 and (c) as implied by height statistics used in OI.

The correlations of the rotational part of the wind and of the geopotential look reasonable, although are slightly broader than in Fig 16 of HL86 and Fig 10 of LH86. This can be explained by the fact that HL86 and LH86 statistics are computed over North America. The vertical structure functions used in the operational OI are e.g. broader over the oceans. The vertical correlations of the divergent part of the wind are quite sharp, but these are known to be sharper than the ones for the rotational part (HL86).

The only inconsistency found is between the temperature results and the vertical temperature correlations of the OI over land. There is less discrepancy with the OI vertical correlations over the ocean even if they are still too sharp. These are derived by differentiation of functionally fitted height statistics which have been artificially sharpened for the analysis of wind measurements (Fig 11.c). These are much sharper than our results and also exhibit negative side-lobes close to the main peak, a direct consequence of differentiating rather sharp height statistics. Attempts have been made below to explain this inconsistency.

Taking the wavenumber range $n = 10$ to $n = 100$ ("synoptic-scale"), vertical correlations were computed from the 48-24 hour forecast statistics. In figure 12 results for the rotational part of the wind (12.a), the stream function (12.b) and the geopotential (12.c) are presented. If the geostrophic assumption is valid ($\psi = \phi/f$), the same statistics for streamfunction and geopotential should be observed. Comparing Fig 12.b and 12.c, streamfunction correlation structure is seen to be slightly sharper than that for geopotential. This suggests there is some imbalance between wind and geopotential in the forecast error statistics.

Also implicit in the derivation of temperature correlations from the OI statistics is the assumption of separability (i.e. same vertical correlation for each horizontal scale). To investigate the separability assumption, one can introduce a vertical correlation matrix defined separately for each term of the horizontal expansion as in HL86. In our notation, the covariance between two points separated by a distance r on the horizontal at two different horizontal levels Zi and Zj can be written as

$$
\overline{\psi(x,Zi)\,\psi(x + r,Zj)} = \sum_{n=o}^{N} (P_n(Zi)\, P_n(Zj))^{\frac{1}{2}}\, C_n(Zi,Zj)\, \frac{P_n^o(r)}{\sqrt{2n + 1}}
$$

where $P_n(Zi) = \sum_{m=-n}^{n} \overline{\psi_n^m(Zi)\ \psi_n^m(Zi)^*}$

Fig 12(a)   Vertical correlations for differences between 24hr and 48hr forecasts for a range of levels computed from all wavenumbers from n=10 to n=100 for the rotational part of the wind.

23

Fig 12(b)   Vertical correlations for differences between 24hr and 48hr forecasts for a range of levels computed from all wavenumbers from n=10 to n=100 for streamfunction.

24
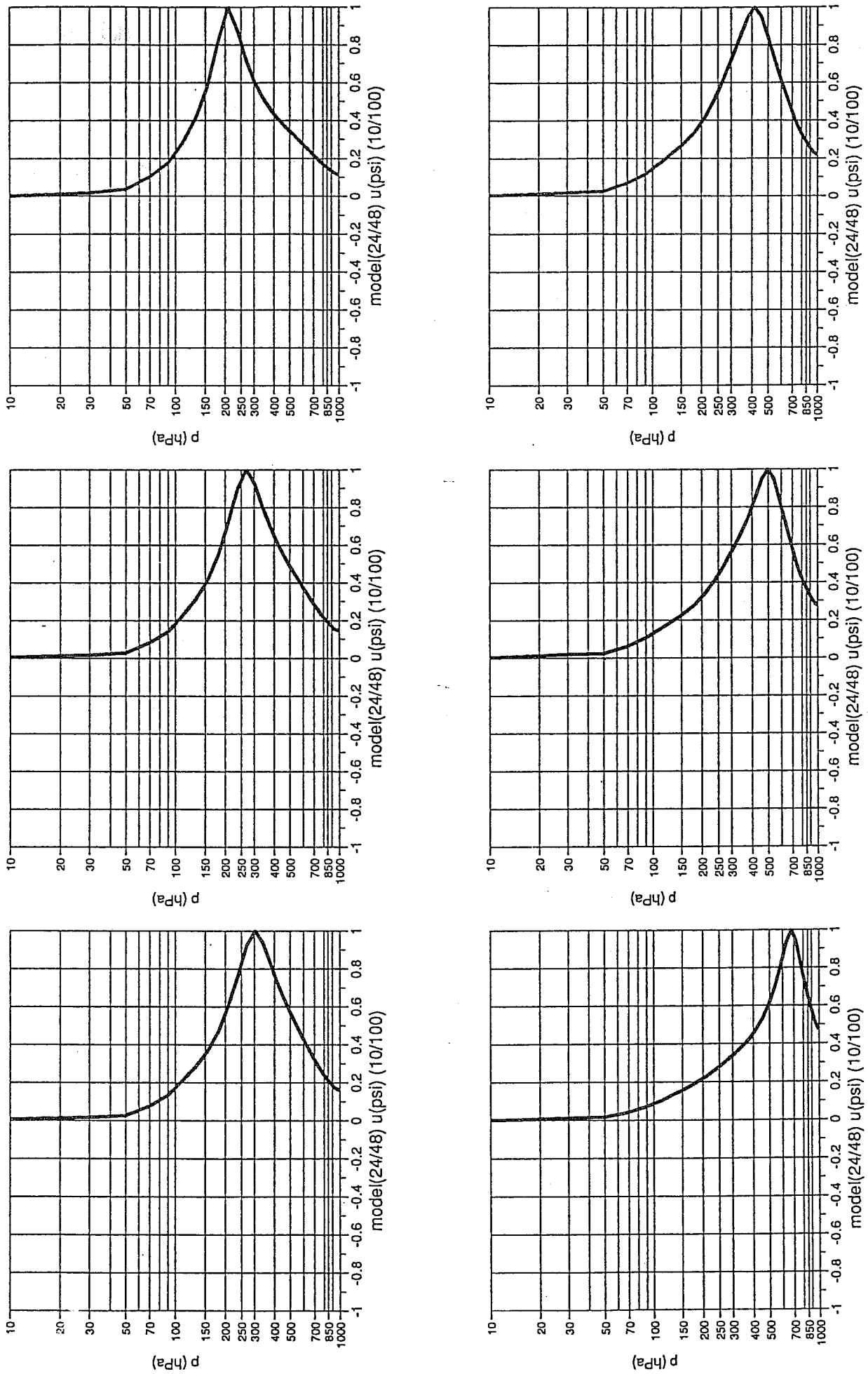
Fig 12(c) Vertical correlations for differences between 24hr and 48hr forecasts for a range of levels computed from all wavenumbers from n=10 to n=100 for geopotential.
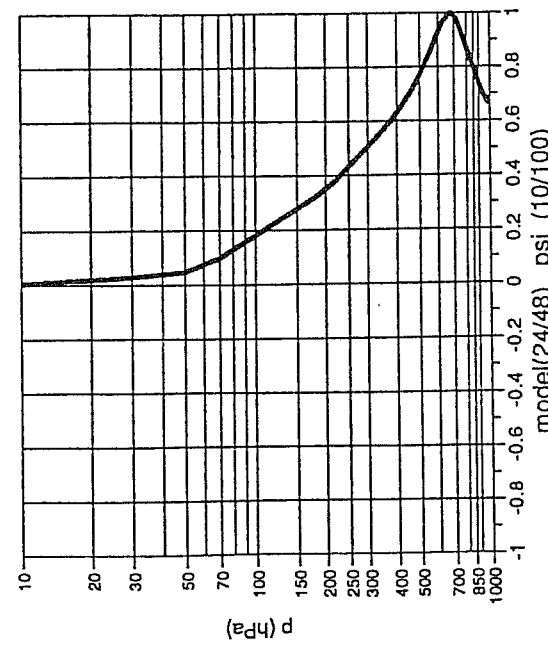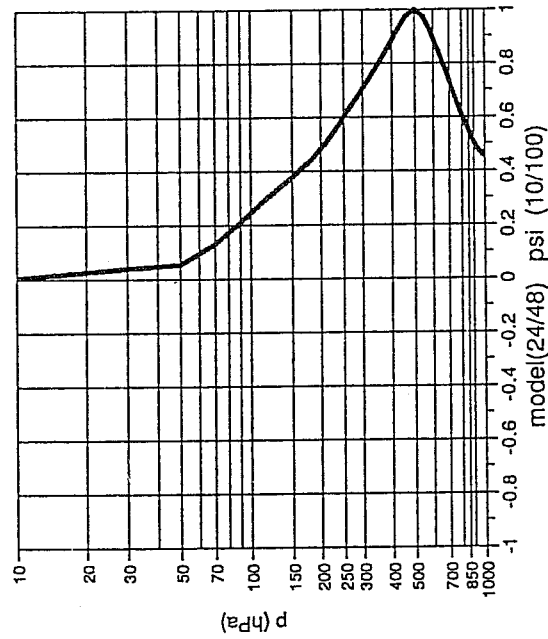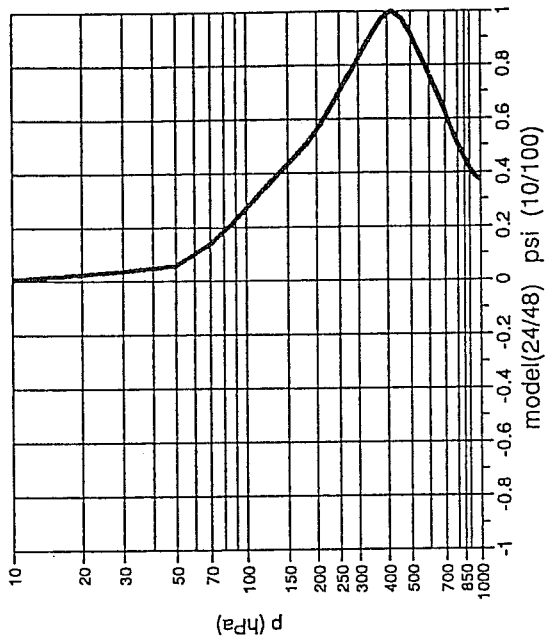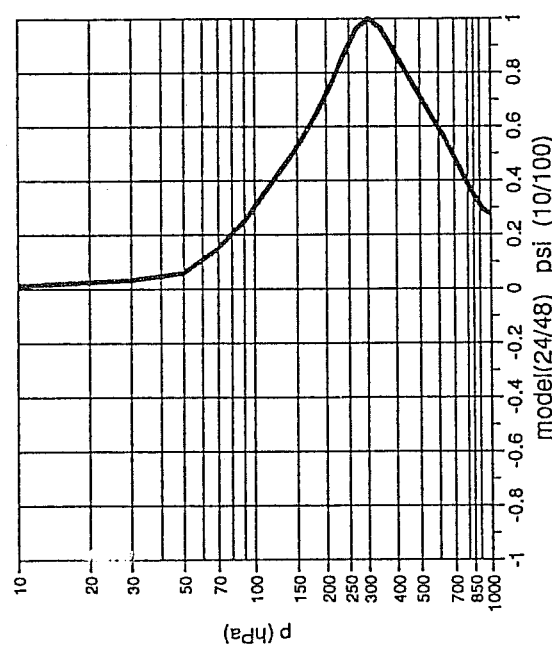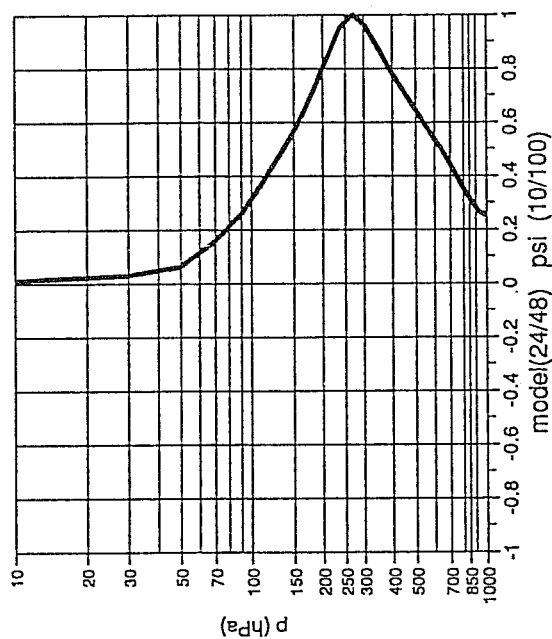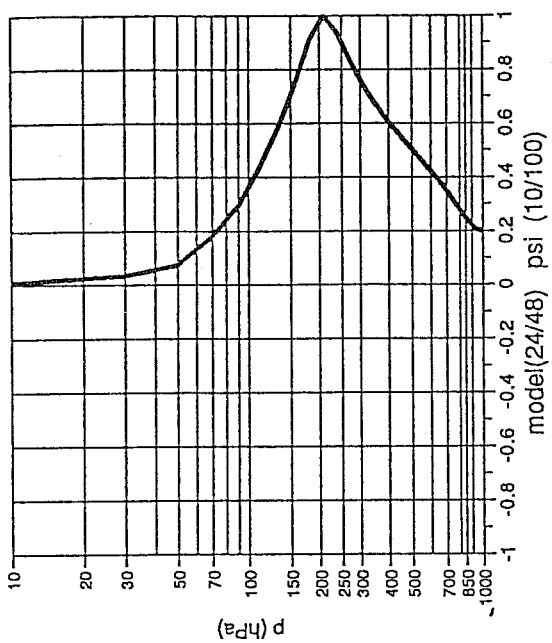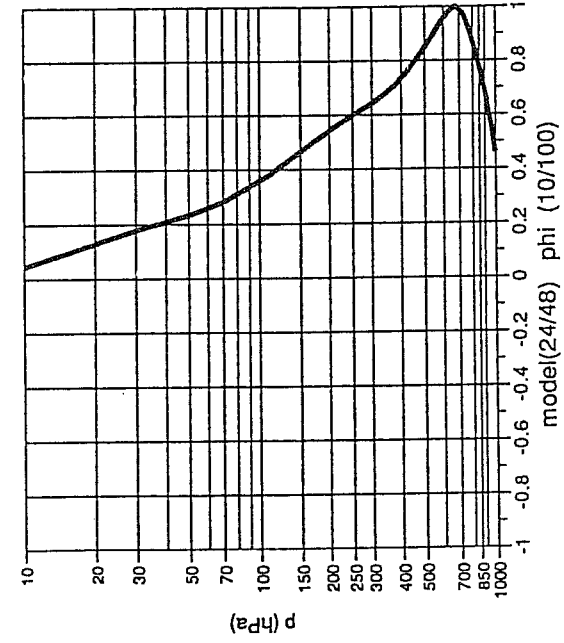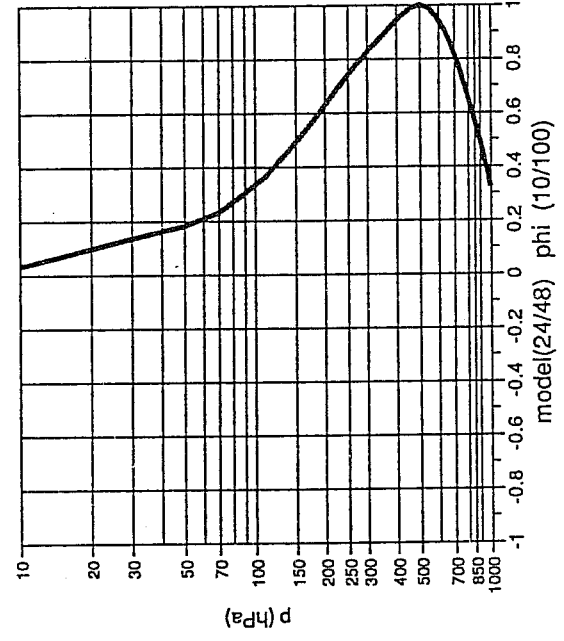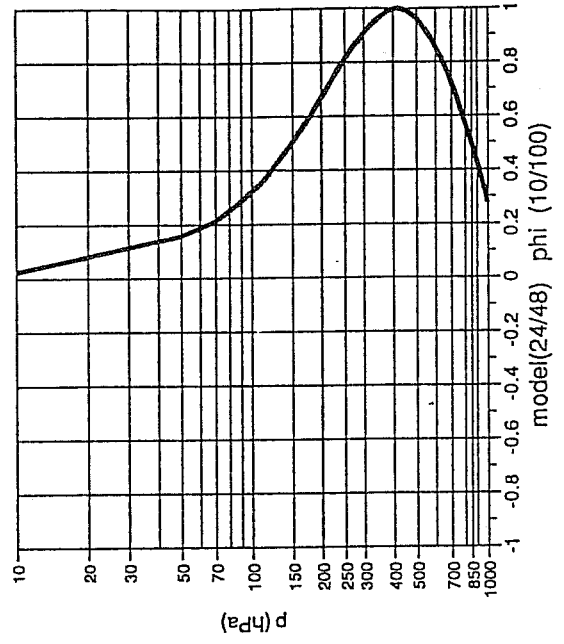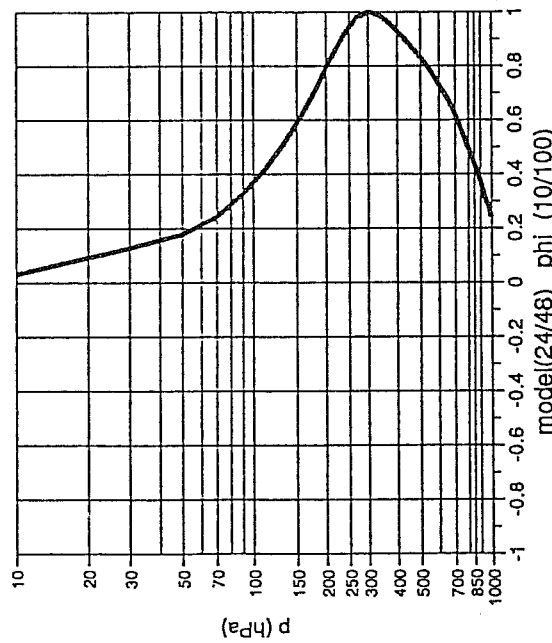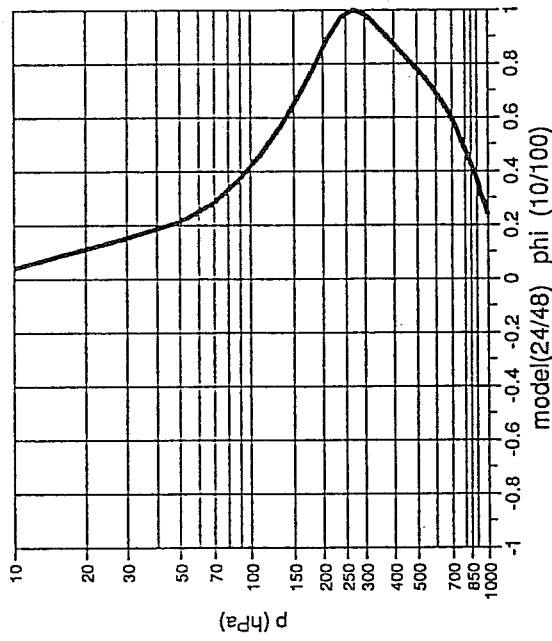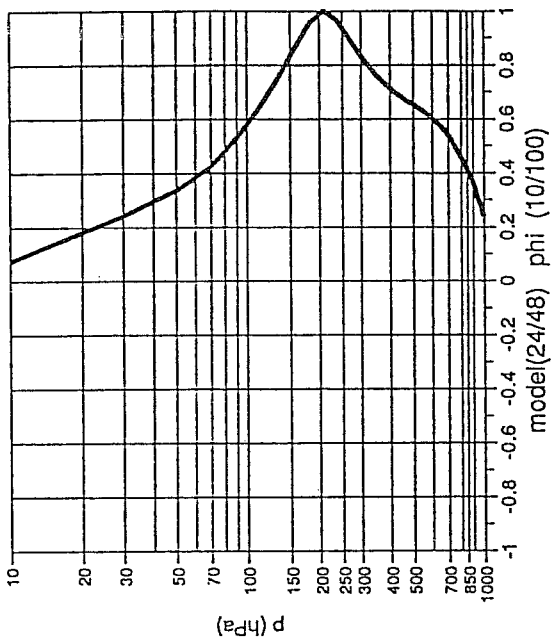
25

$$P_n(Zj) = \sum_{m=-n}^{n} \overline{\psi_n^m(Zj) \; \psi_n^m(Zj)^*}$$

$$\text{and} \quad C_n(Zi,Zj) = \frac{\sum_{m=-n}^{n} \overline{\psi_n^m(Zi) \; \psi_n^m(Zj)^*}}{\left(P_n(Zi)P_n(Zj)\right)^{\frac{1}{2}}}$$

If the vertical correlation matrices $C_n(Zi,Zj)$ are independent of n and equal to a matrix $C(Zi,Zj)$, the

expansion becomes $\overline{\psi(x,Zi)\psi(x+r,Zj)} = C(Zi,Zj) \sum_{n=o}^{N} \left(P_n(Zi)P_n(Zj)\right)^{\frac{1}{2}} \dfrac{P_n^o(r)}{\sqrt{2n+1}}$.

Furthermore, if the horizontal spectra $P_n(Zi)$ are independent of level and equal to P_n, the expression is

fully separable $\overline{\psi(x,Zi)\psi(x+r,Zj)} = C(Zi,Zj) \sum_{n=o}^{N} P_n \dfrac{P_n^o(r)}{\sqrt{2n+1}}$. The variation of the vertical correlation

matrices $C_n(Zi,Zj)$ with respect to n can be investigated.

In Fig 13 the vertical correlation matrices for the vorticity part of the wind (panel a) and the geopotential (panel b) are shown summed over the wave number ranges $n = 0$ to 10, $n = 10$ to 20, $n = 20$ to 30, $n = 30$ to 40, $n = 40$ to 50 and $n = 50$ to 60. The sharpening of the structure when going to smaller scales is striking for both variables, which questions the validity of the separability hypothesis. This is consistent with the findings in HL86 and LH86, although the dispersion was less marked. A lack of separability is also seen in the vertical correlations for the rotational part of the wind and for the streamfunction being different. Thus, even assuming a perfect geostrophic balance, vertical correlation structure summed over all wavenumbers for wind is sharper than that for geopotential. This result was found in *Phillips* (1986) and could be explained for a theoretical ensemble of geostrophic modes.

The main (and easy to implement) part of the non-separability is the dependency of the correlation matrices with the total wavenumber n. As structures become sharper in the vertical for smaller horizontal scales, this can be seen as a 3D-isotropy. An influence from all the three factors described above (namely, our wind statistics being broader than those of OI, slight imbalance between wind and geopotential and a lack of separability) to explain the differences between our results for temperature and the ones derived from the

Fig 13(a) Vertical correlations for differences between 24hr and 48hr forecasts for level 250 hPa computed for various ranges of wavenumbers for the rotational part of the wind.
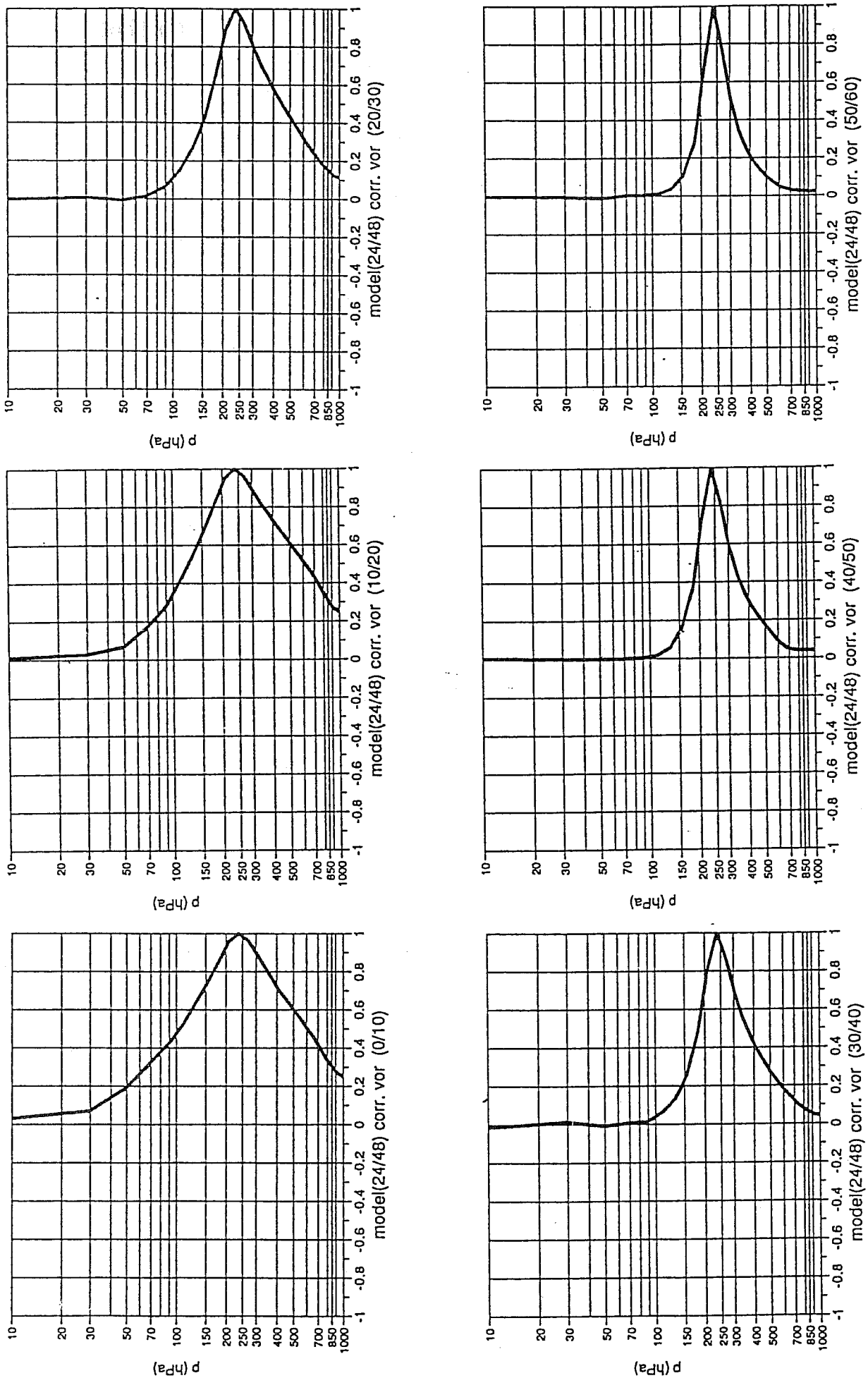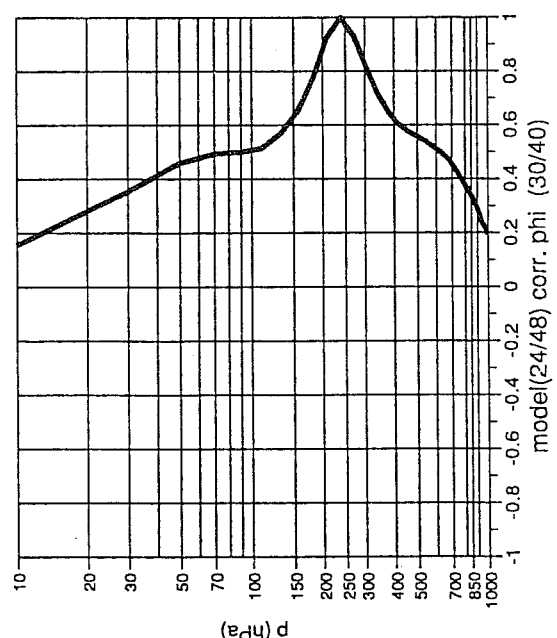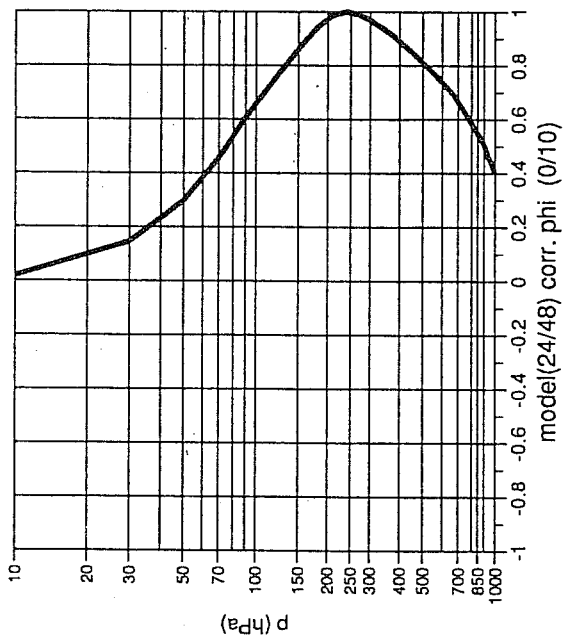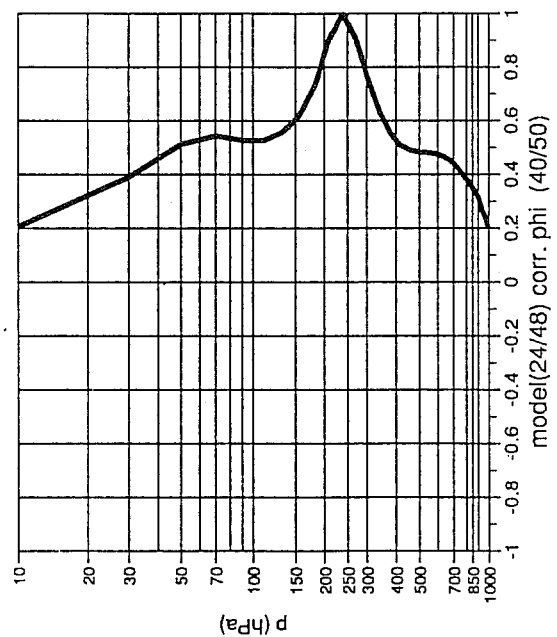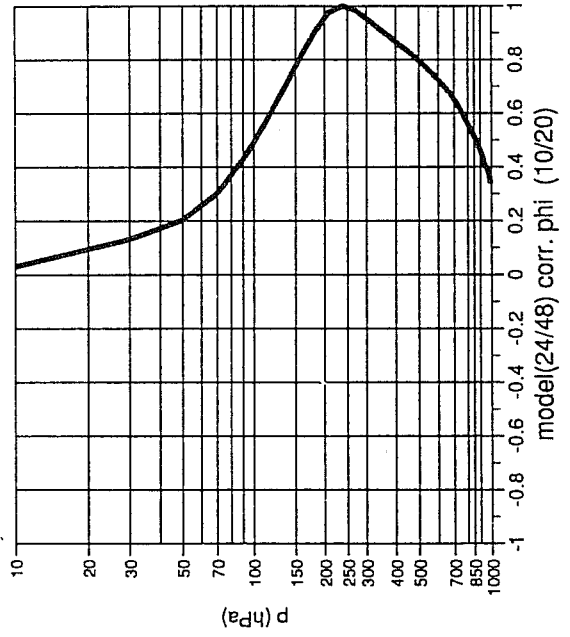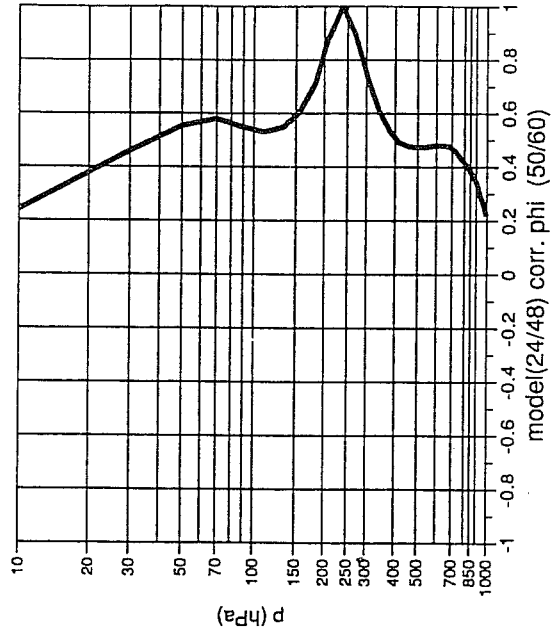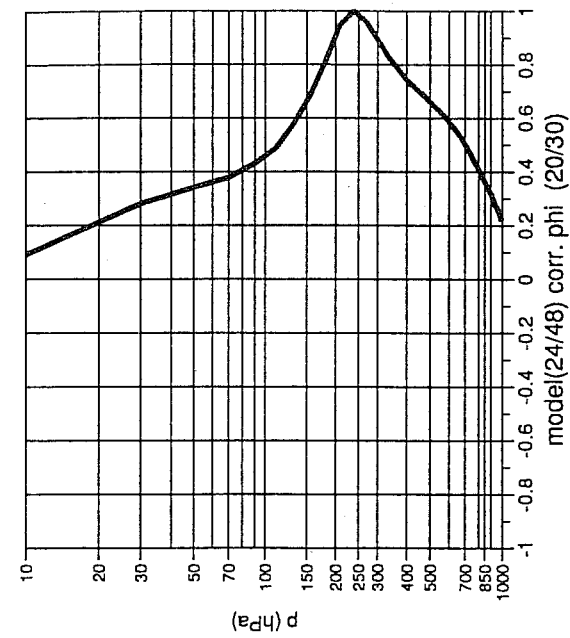
Fig 13(b)   Vertical correlations for differences between 24hr and 48hr forecasts for level 250 hPa computed for various ranges of wavenumbers for geopotential.

28

OI. As a remark, another proof of non-separability can be found in the fact that the slopes of the horizontal spectra in the synoptic scales are different for temperature (around -2, -3) and height (approximately -4).

4.   SUMMARY

The first part of this study used the departures of first guess radiance from satellite measured values to investigate the slope of the forecast error spectra for large scales (i.e the variation of error with wavenumber). For the temperature spectra it was found that this slope increases for the lower atmospheric levels (consistent with less energy in the very large scales close to the ground).

These results were generally confirmed by the second part of this study which used the differences between a 24 hour forecast and a 48 hour forecast valid at the same time (NMC method) to investigate the characteristics of forecast error. Furthermore, the results obtained with the NMC method agree well with other observational studies. As far as the horizontal spectra are concerned, the increase of length-scale with altitude is in agreement with results of HL86 and LH86 and of *Phillips* (1986), the slopes in the small scales show more and more importance of the small scales close to the ground. The linear balance between wind and geopotential seems to be reasonably valid in the range $n > 10$ whereas it is not in the very large scales ($n < 10$). Spectra for vorticity and divergence are seen to be quite different, the divergence spectrum having more energy in the very fine scales than the vorticity spectrum. The best solution for 3D-VAR appears to be to use different spectra for vorticity and for divergence. Different spectra for the same variable according to the horizontal level could also be used.

As far as the vertical correlations are concerned, results for the rotational part of the wind, the divergent part of the wind and the geopotential agree reasonably well with HL86, LH86, although our correlation structures are slightly broader. Temperature correlations agree well with statistics from the satellite section, and these results have been used to revise 1D-VAR (the impact is currently being evaluated, memo R43.12/JE/AD/68/SD from 1/4/1993). Three reasons have been identified why the temperature correlations are broader than those implied by OI. Namely, statistics are not in strict balance, our wind statistics are slightly broader, and more importantly, the separability assumption is not valid. The breakdown of the separability assumption (more marked than observed in HL86 and LH86) suggests that it might be useful in 3D-VAR to use different vertical correlation matrices for different sets of wavenumbers.

Although there is no rigorous justification why the NMC method should represent forecast error statistics, it seems to give reasonable results which are in agreement with previous observational studies. This agreement gives us some confidence to use the greater flexibility of the NMC method to investigate characteristics of forecast error beyond the scope of conventional observational studies. In particular, it has highlighted potential weaknesses of the current 3D-VAR formulation (i.e. same length-scale on the vertical,

same horizontal spectra for vorticity and divergence, same vertical correlation for different variables). It is hoped that the NMC method will allow further refinements of the statistics used in the variational scheme.

Acknowledgements

References

Abramowitz, M and I A Stegun, 1965: Handbook of mathematical functions. Dover Publications Inc, New York. 1045 pp.

Balgovind, R, A Dalcher, M Ghil and E Kalnay, 1983: A stochastic-dynamic model for the spatial structure of forecast error statistics. Mon Wea Rev., Vol 111, 701-722.

Bartello, P and H L Mitchell, 1992: A continuous three-dimensional model of short-range forecast error covariance. Tellus, 44A, 217-235.

Boer, G J, 1983: Homogeneous and isotropic turbulence on the sphere. J Atmos Sci, Vol 40, 154-163.

Eyre, J R, 1992: A bias correction scheme for simulated TOVS brightness temperatures. ECMWF Technical Memorandum No. 186.

Hildebrand, F B, 1976: Advanced calculus for applications. Prentice-Hall Inc, Englewood Cliffs, New Jersey. 733 pp.

Hollingsworth, A and P Lönnberg, 1986: The statistical structure of short-range forecast errors as determined from radiosonde data. Part I: The wind field. Tellus, 38A, 111-136.

Lönnberg, P and A Hollingsworth, 1986: The statistical structure of short-range forecast errors as determined from radiosonde data. Part II: The covariance of height and wind errors. Tellus, 38A, 137-161.

Lönnberg, P, 1988: Developments in the ECMWF analysis system. Proceedings of ECMWF Seminar "Data assimilation and the use of satellite data", Vol I, 75-120.

McNally, A, 1993: Technical memo, currently being written.

Parrish, D F and J C Derber, 1992: The National Meteorological Center's Spectral Statistical Interpolation Analysis System. Mon Wea Rev, Vol 120, 1747-1763.

Phillips, N A, 1986: The spatial statistics of random geostrophic mode and first-guess errors. Tellus, 38A, 314-322.

Rochas, M J, P Courtier, K Yessad and Y Bouteloup, 1991: Rotations in spectral space. Beitr Phys Atmosph, Vol 64, No. 3, 201-206.

Under the homogeneity and isotropy assumption, the correlation between two points $((\lambda,\mu); (\lambda',\mu'))$ for a meteorological variable ϕ is only a function of the distance between the points:

$$f(r) = \overline{\left(\frac{\phi(\lambda,\mu)-\overline{\phi(\lambda,\mu)}}{\sigma_\phi(\lambda,\mu)}\right) \cdot \left(\frac{\phi(\lambda',\mu')-\overline{\phi(\lambda',\mu')}}{\sigma_\phi(\lambda',\mu')}\right)} = \overline{\psi(\lambda,\mu).\psi(\lambda',\mu')}$$

where

- $\overline{X(\lambda,\mu)}$ represents the expectation of X, taken as the time-average of X at location (λ,μ).

- $\sigma_\phi^2(\lambda,\mu) = \overline{(\phi(\lambda,\mu)-\overline{\phi(\lambda,\mu)})^2}$ is the variance of the field

- $\psi(\lambda,\mu) = \dfrac{\phi(\lambda,\mu)-\overline{\phi(\lambda,\mu)}}{\sigma_\phi(\lambda,\mu)}$ is the normalised departure.

1.   FORMULATION IN TERMS OF BESSEL SERIES

In *Hollingsworth and Lönnberg* (1986) and *Lönnberg and Hollingsworth* (1986) (LH86) a curve $f(r)$ is derived from accumulated statistics over the Northern American network and fitted by a series of Bessel functions:

$$f(r) = \sum_{n=0}^{N} \phi_n^2 \, J_o\left(k_n\frac{r}{D}\right)$$

The wavenumbers k_n are determined by the requirement of vanishing radial derivative at distance D ($J_o'(k_n) = 0$, equation 175b p 226 of *Hildebrand*, 1976).

The pair of spectral transforms is then written as

$$f(r) = \sum_{n=0}^{N} \phi_n^2 \, J_o\!\left(k_n \frac{r}{D}\right) \qquad (1)$$

$$\phi_n^2 = \frac{2}{J_o^2(k_n)} \int_o^D f(r) \, J_o\!\left(k_n \frac{r}{D}\right) \frac{r}{D} \frac{dr}{D} \qquad (2)$$

(2) Comes from section 11.4.5, p 485 of *Abrawowitz and Stegun* (1965): $\int_o^D J_o\!\left(k_n \frac{r}{D}\right)^2 \frac{r}{D} \frac{dr}{D} = \frac{1}{2} J_o^2(k_n)$

or Eq. 185.b, p 229 of *Hildebrand* (1976).

LH86 define the spectrum as: $S_n = \phi_n^2 \, J_o^2(k_n) = 2 \int_o^D f(r) \, J_o\!\left(k_n \frac{r}{D}\right) \frac{r}{D} \frac{dr}{D}$. As noted by *Bartello and*

Mitchell (1992), this spectrum corresponds to what is called a "modal spectrum" which can more easily be

seen using continuous notations.

The transform pair is then $\begin{cases} f(r) = \int_o^\infty S(k) \, J_o(kr) k \, dk \\ S(k) = \int_o^\infty f(r) \, J_o(kr) r \, dr \end{cases}$.

As in *Balgovind et al.* (1983), $S(k)$ can be rewritten with respect to a couple of wavenumbers (a,b) on the

plane such as $k^2 = a^2 + b^2$, then $S(k) = S(a,b) = \frac{1}{2\pi} \int_{-\infty}^{+\infty} \int_{-\infty}^{+\infty} f(x,y) e^{iax} e^{iby} dx dy$. $S(k)$ then corresponds

to the contribution of the particular mode (a,b) to the total correlation. The correlation at zero-distance

$f(o) = 1 = \int_o^\infty S(k) k \, dk$.

2. FORMULATION IN TERMS OF LEGENDRE POLYNOMIA

If one develops $f(r)$ in terms of Legendre Polynomia

$$f(r) = \sum_{s=0}^{N} a_s P_s^0(\gamma) \qquad \begin{cases} r = a\theta \\ \gamma = \cos\theta \end{cases} \text{ where } \theta \text{ is the angle between the pole and the point.}$$

and if one uses the spectral transforms involving spherical harmonics for the field ψ itself, following *Boer* (1983)

$$\begin{cases} \psi(\lambda,\mu) = \sum_{n=0}^{N} \sum_{m=-n}^{n} \psi_n^m \, Y_n^m(\lambda,\mu) \\ \psi_n^m = \dfrac{1}{4\pi} \int_0^{2\pi} \int_{-1}^{1} \psi(\lambda,\mu) Y_n^{-m}(\lambda,\mu) d\lambda d\mu \end{cases}$$

$$f(r) = \overline{\psi(\lambda,\mu)\cdot\psi(\lambda',\mu')} = \overline{\left(\sum_{n,m} \psi_n^m Y_n^m(\lambda,\mu)\right)\left(\sum_{n',m'} \psi_{n'}^{m'} Y_{n'}^{m'}(\lambda',\mu')\right)}$$

$$= \sum_{n,m} \sum_{n',m'} \overline{\psi_n^m \psi_{n'}^{-m'}} Y_n^m(\lambda,\mu) Y_{n'}^{-m'}(\lambda',\mu')$$

Equivalently $\overline{\psi_n^m \psi_{n'}^{-m'}}$ can be expressed as a function of $f(r)$

$$\overline{\psi_n^m \psi_{n'}^{-m'}} = \overline{\left(\frac{1}{4\pi}\iint \psi(\lambda,\mu) Y_n^{-m}(\lambda,\mu) d\lambda d\mu\right) \cdot \left(\frac{1}{4\pi}\iint \psi(\lambda',\mu') Y_{n'}^{-m'}(\lambda',\mu') d\lambda' d\mu'\right)}$$

$$= \left(\frac{1}{4\pi}\right)^2 \iiiint \overline{\psi(\lambda,\mu)\psi(\lambda'\mu')} \, Y_n^{-m}(\lambda,\mu) \, Y_{n'}^{-m'}(\lambda',\mu') \, d\lambda d\mu d\lambda' d\mu'$$

$$= \left(\frac{1}{4\pi}\right)^2 \iiiint \left(\sum_{s=0}^{N} a_s P_s^0(\gamma)\right) Y_n^{-m}(\lambda,\mu) \, Y_{n'}^{-m'}(\lambda',\mu') \, d\lambda d\mu d\lambda' d\mu'$$

Using $\dfrac{1}{4\pi}\iint \sqrt{2s+1} \, P_s^0(\gamma) Y_{n'}^{-m'}(\lambda',\mu') \, d\lambda' d\mu' = \delta_s^{n'} \, \delta_m^{m'} \, Y_{n'}^{-m'}(\lambda,\mu)$ (*Rochas et al*, 1991; *Boer*, 1983)

$$\overline{\psi_n^m \psi_{n'}^{-m'}} = \frac{1}{4\pi}\iint \frac{a_{n'}}{\sqrt{2n'+1}} \; Y_n^m(\lambda,\mu)Y_{n'}^{-m'}(\lambda,\mu) \; d\lambda d\mu$$

we find

$$\overline{\psi_n^m \psi_{n'}^{-m'}} = \delta_n^{n'}\delta_m^{m'}\frac{a_{n'}}{\sqrt{2n'+1}} = \begin{cases} \dfrac{a_n}{\sqrt{2n+1}} & \text{if } (n,m) = (n',m') \\ 0 & \text{if } (n,m) \neq (n',m') \end{cases}$$

These are the useful relations to define the correlations in spectral space from correlations in grid-point space.

Expressing the correlation at zero-distance

$$<\overline{|\psi|^2}> = \frac{1}{4\pi}\iint \overline{\psi(\lambda,\mu)\psi(\lambda,\mu)} \; d\lambda d\mu$$

$$= \frac{1}{4\pi}\iint \sum_{nm}\sum_{n'm'} \overline{\psi_n^m\psi_{n'}^{-m'}} \; Y_n^m(\lambda,\mu)Y_{n'}^{-m'}(\lambda,\mu) \; d\lambda d\mu$$

$$= \frac{1}{4\pi}\iint \sum_{nm} \overline{|\psi_n^m|^2} \; Y_n^m(\lambda,\mu) \; Y_n^{-m}(\lambda,\mu) \; d\lambda d\mu$$

$$<\overline{|\psi|^2}> = \sum_{nm}\overline{|\psi_n^m|^2} = \sum_{n=0}^{N}\left(\sum_{m=-n}^{n}\frac{a_n}{\sqrt{2n+1}}\right)$$

$$<\overline{|\psi_n^m|^2}> = \sum_{n=0}^{N}(2n+1)\overline{|\psi_n^m|^2} = \sum_{n=0}^{N}a_n\sqrt{2n+1} = \sum_{n=0}^{N}P_n$$

$P_n = a_n\sqrt{2n+1}$ is the energy of the correlation, in particular two-dimensional wavenumber n, also called "Power" spectrum.

Remark: equivalently it can be seen from:

$$f(r) = \sum_{s=0}^{N} a_s \, P_s^o(\gamma)$$

$$f(o) = \sum_{s=0}^{N} a_s\sqrt{2s+1} = \sum_{s=0}^{N} P_s$$

In terms of a couple of wavenumbers $(n-m,m)$, the model spectrum would be written $P_{n,m} = \dfrac{a_n}{\sqrt{2n+1}} = \dfrac{P_n}{2n+1}$

A4

3. ASYMPTOTIC EQUIVALENCE BETWEEN THE TWO FORMULATIONS

In one case: $f(r) \sim \sum_{n=0}^{N} \phi_n^2 J_o\left(k_n \frac{r}{D}\right)$

in the other: $f(r) \sim \sum_{n=0}^{N} a_n P_n^o(\gamma)$ with $\gamma = \cos\theta = \cos\frac{r}{a}$

in terms of non-normalised Legendre polynomia:

$$f(r) \sim \sum_{n=0}^{N} a_n\sqrt{2n+1}\, P_n(\gamma)$$

In the limit $n \to +\infty$, $\lim_{n\to\infty} P_n\left(\cos\frac{x}{n}\right) = J_o(x)$

from Eq. 9.1.71 p 362 for ($\mu = 0$ of *Abramowitz and Stegun*, 1965)

$$P_n(\gamma) = P_n\left(\cos\frac{r}{a}\right) \sim J_o\left(\frac{nr}{a}\right)$$

we then have $f(r) \sim \sum a_n\sqrt{2n+1}\, J_o\left(\frac{nr}{a}\right)$

Identification between the two formulas gives: $\begin{cases} \dfrac{nr}{a} \sim \dfrac{k_n r}{D} \\ \phi_n^2 \sim a_n\sqrt{2n+1} \end{cases}$

$$\begin{cases} f(r) \sim \sum \phi_n^2 J_o\left(\dfrac{k_n r}{D}\right) \text{ with } S_n = \phi_n^2 J_o^2(k_n) \\ f(r) \sim \sum a_n\sqrt{2n+1} J_o\left(\dfrac{nr}{a}\right) \text{ with } P_n = a_n\sqrt{2n+1} \end{cases}$$

The multiplying factor between S_n and P_n is $J_o^2(k_n)$ and we know that $J_o^2(k_n) \sim \dfrac{2}{\pi k_n} \sim \dfrac{2}{\pi n}$ from Eq. 9.2.28

p 365 of Abramovitz-Stegun.

We then have $S_n \sim \dfrac{P_n}{n}$.

4. GEOSTROPHIC RELATIONSHIP

$$KE_n^m = -\frac{1}{2}\left(\xi_n^m \Delta^{-1}\xi_n^m + D_n^m \Delta^{-1} D_n^m\right), \text{ with } \xi = \Delta\psi.$$

If there is not divergent part $\quad KE_n^m = -\frac{1}{2}\,\xi_n^m\Delta^{-1}\xi_n^m$

Replacing ξ_n^m by $-\dfrac{n(n+1)}{a^2}\psi_n^m$ and identifying ψ_n^m with $\dfrac{1}{f}\times\phi_n^m$, we get $KE_n^m = +\dfrac{n(n+1)}{2\,f^2\,a^2}\,\phi_n^{m^2}.$